Cure Kinetics Study of Two Part Epoxy Resin and the Effect on Characterization of Thermal Barrier Coatings

Sunny Chang

Thesis submitted to the faculty of the Virginia Polytechnic Institute and State University
in partial fulfillment of the requirements for the degree of

Master of Science
In
Materials Science and Engineering

Gary R. Pickrell, Chair
Alan P. Druschitz
Dan S. Homa
Brian L. Scott

April 16, 2015
Blacksburg, VA

Keywords: Thermal Barrier Coatings, Curing Kinetics, Two-Part Epoxy, TBC Characterization, Variability

Cure Kinetics Study of Two Part Epoxy Resin and the Effect on Characterization of Thermal Barrier Coatings

Sunny Chang

Abstract

The aerospace industry strives to develop new methods of refining gas turbine engines by increasing power and thermal efficiencies while simultaneously reducing cost. Turbine engines operate under high temperatures and therefore thermal barrier coatings (TBCs) composed of yttria-stabilized zirconia (YSZ) play an important role in improving the performance of the components that make up the engine. Failure of the TBC could lead to catastrophic events, thus requiring consistent and accurate characterization for supplier qualification and production quality assurance. However, due to porosity and the anisotropic behavior of the coating and variability in processing of TBCs, consistent characterization has proven to be extremely challenging. One of the reoccurring issues is the inconsistency in measuring percent porosity, which stems from the difficulty in distinguishing filled pores from damaged, unfilled voids.

Sample preparation of TBCs involves sectioning, mounting, grinding, polishing, and characterization. Eliminating variability in characterization begins with mounting which is a critical step to protect the surface integrity and edge retention of the coating during grinding and polishing. The curing kinetics of a slow cure two part epoxy was investigated and the TBC samples were mounted and cured at heating rates of 2, 5, and 10 °C/min to 55 °C and 70 °C. Grinding and polishing procedures simulated industry practices followed by characterization with optical microscopy. Results showed that heating rates of 2 °C/min to 55 °C and 70 °C have the best impregnation properties while uncontrolled or high heating rates of 10 °C/min had an increase in the amount of pullouts and lack of infiltration from the epoxy. The curing kinetics of the epoxy needs to be controlled to eliminate the ambiguity of filled and unfilled pores.

Acknowledgements

I am extremely thankful towards my advisor Dr. Gary Pickrell for the opportunity to be part of his research group and for his guidance and encouragement throughout my research work. My appreciation goes out to the rest of my committee: Dr. Alan Druschitz, Dr. Dan Homa, and Dr. Brian Scott for their patience, support, and advice.

I would like to thank the Commonwealth Center for Advanced Manufacturing (CCAM) particularly Ben Zimmerman, for many stimulating discussions about TBCs and for supplying samples to make this research possible. My sincere thanks to Mike Keeble from Buehler and Roy McIntyre from Rolls Royce for their guidance throughout my time at CCAM and for their expertise on sample preparation of TBCs.

Many thanks to the members of Virginia Tech Center for Photonics Technology (CPT) who allowed me to use the equipment and tolerated quite a bit of noise pollution. I am thankful to Dr. Thomas Staley from the department of Materials Science and Engineering (MSE) for his time and assistance in equipment training and data analysis. I would also like to thank Dr. Bruce Orler from the department of Chemistry for his willingness to assist me in understanding my data and Stephen McCartney from ICTAS Nanoscale Characterization and Fabrication Laboratory (NCFL) who assisted me with the ESEM. I would like to thank my colleagues who helped me through my experimental work, Cary Hill, Andre Stevenson, and Adam Floyd from MSE. By God's grace was I able to get through this endeavor and I thank my family and friends who continue to support and pray for me.

The author would like to acknowledge financial support from the National Energy Technology Lab (NETL) at the U.S. Department of Energy (DOE) under contract DE-FE0012274.

Disclaimer

Table of Contents

List of Figures

List of Tables

1. Introduction

Gas turbine engines provide efficient and reliable means of power generation. The power generation is produced by burning an air-fuel mixture which means gas turbines are a type of internal combustion engine. The idea of this engine dates back to 1791 by John Barber who designed the turbine to power a horseless carriage [1]. Today, gas turbines are used to produce thrust in aviation as well as electricity in industrial plants, automobiles, and marine applications. Typically, gas turbines used to provide electricity are fired on natural gas. However, in aviation the turbine may be constructed to run on petroleum-based fuels and synthetic fuels [2]. An advantage that gas turbines in aerospace have over other types of engines is the high power to weight ratio and the ability to provide power at times of peak demand, which in this case, is during take-off and landing. Major manufacturers of aero-engines (Rolls Royce, General Electric, and Pratt and Whitney) strive to find new ways of improving turbines by increasing power and thermal efficiencies while simultaneously reducing cost.

1.1 Gas Turbine Overview

Although turbine engines come in a variety of shapes and sizes, they share a common core design. The three main sections in any turbine engine design are the compressor, combustor, and turbine [3] as shown in Figure 1 below.

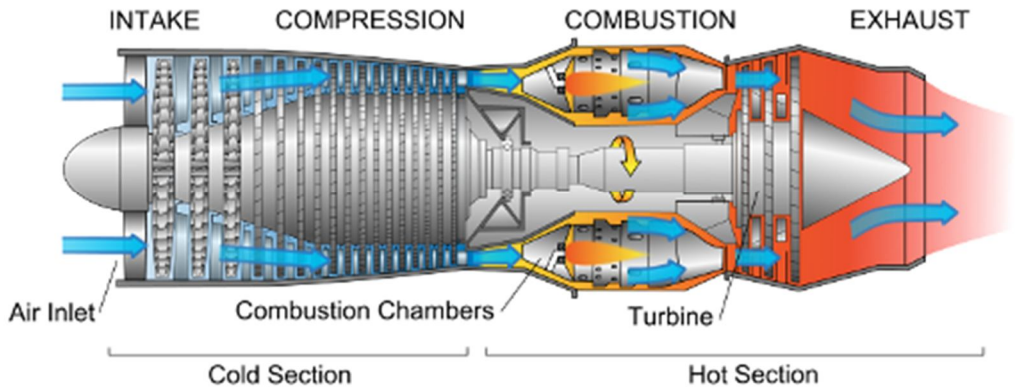

Figure 1: Schematic of gas turbine engine [3], Schematic has been released by J. Dahl, *Wikipedia*, [online] 16 December 2007, http://en.wikipedia.org/wiki/File:Jet_engine.svg into public domain, 2015

The front of the engine begins with fan blades that push air through to the first component of the turbine engine core, the compressor. In the compressor, rotating blades continue to compress the air into a smaller area, thus increasing the air pressure. The high pressure increases the potential energy of air and continues to flow through the combustion chamber. In the combustion chamber, the air is heated by fuel combustion resulting in an increase in volume. Gas produced in the combustion chamber expands through the turbine section, causing the turbine blades attached to an axle to rotate. The same axle is attached to the fan and compressor and therefore, the rotation of the turbine blades help to turn the fan and the compressor. Finally the combusted gas exits through the exhaust, producing thrust from the hot air twice the speed of the initial cold air.

1.2 Operation Conditions and Materials Selection

When both technical and business objectives intertwine, the design of the gas turbine engine becomes complex. The desire to reduce cost while increasing engine power and efficiency needs to be balanced. Gas turbine engine components are subject to harsh

environments such as: mechanical loading conditions, high temperatures, and corrosive and/or erosive media [4]. Thus, cost considerations are not only for the initial cost, but the life cycle cost as well. The rationale behind selecting a material is the ability to minimize cost while meeting the product performance targets [2].

There are a number of factors that influence the final cost of the material. One component is the ability to revert scrap to usable secondary metal. If reverting scrap is not an option, another contributing cost factor is the utilization of raw materials and how easily these materials can be forged, cast, and machined for quality consistency [2]. Selecting the right material is critical to maximizing the turbine fuel efficiency and the lifetime.

How efficient the engine is begins with the first component of the engine, the fan blades. Fan blades are exposed to the environment and must be designed to withstand impacts from objects up to the size of birds as well as extreme temperatures and weather. Therefore, fan blades need to be large to increase air flow, yet light and balanced with its strength [5] that allows resistance to mass flow of air around 72 tonnes/min and a centripetal force of 900 kN [6]. Titanium 6/4 (Ti 6/4) is the industry standard fan blade material with a strength to weight ratio of approximately 264 kN*m/kg [7]. Fan blades are made hollow to reduce weight and as a result, fuel consumption. The hollow blades are created by a super plastic forming technique of two metal sheets and then diffusion bonding the halves together [5, 6]. Compared to pure titanium, Ti 6/4 has the same stiffness but is significantly stronger due to the addition of 6% aluminum (Al) and 4% vanadium (V). The additions of Al and V act as phase stabilizers of the pure Ti alpha and

beta phases. At room temperature, pure Ti exhibits an alpha phase, but once heated to temperatures above 882 °C, there is a transformation to the beta phase [8]. The beta phase is stronger than the alpha phase, but much more brittle. Therefore when Al is added to Ti, the Al stabilizes the alpha to beta transformation while the inclusion of V acts as the beta stabilizer which lowers the transformation temperature. As a consequence, Ti 6/4 becomes an alpha/beta alloy with the same stiffness but much stronger, and without the brittleness seen in pure Ti. Fan blades made of Ti 6/4 may be used up to 400 °C [9].

The compressor is divided into two parts: intermediate pressure compressor (IPC) and high pressure compressor (HPC). When air is pushed through to the IPC, the temperature is around 150 °C but increases to around 700 °C when leaving the HPC [5]. Therefore the compressor is predominately comprised of ferrous alloys such as steels and nodular irons. The casing for the inlet portion is typically made of carbon steel or nodular iron while the remainder of the casing is made of low alloy steel. However, due to the high temperatures towards the rear of the compressor, the latter portion of the casing, blades, and vanes are typically made of stainless steel. Stainless steel allows the blades and vanes to withstand higher temperatures and have a higher resistance to oxidation due to the addition of chromium (Cr). The alloying of steel with Cr creates a passivating film of chromium (III) oxide (Cr_2O_3) that prevents oxygen diffusion to the steel surface [10] thus protecting the steel from oxidation.

The combustor and turbine section working temperatures are much higher than the compressor where typical exit temperatures may exceed 2100 °C [5]. Combustor and

turbine parts are typically comprised of nickel (Ni) and cobalt-based superalloys because of their high temperature properties [2, 4]. In the aero industry, superalloys are attractive because of their corrosion resistance and ability to maintain strength and creep resistance properties up to 0.7 times their melting temperature [2]. Superalloy characteristics and performance throughout the turbine engine depend on the crystal structure. Disks are typically polycrystalline and are usually cast, then forged into shape, resulting in high fracture toughness. Turbine blades on the other hand, are usually monocrystalline or single crystal, which allows the blades to have the high creep resistance property due to the absence of grain boundaries. Single crystal blades are manufactured using directional solidification casting [11]. However, the process to increase the creep resistance of the material increases the cost, contributing to difficulty in balancing the technical and business requirements. The ability to select quality materials to meet the demanding requirements of a turbine engine as well as sensible pricing are challenges that the aero industries faces.

1.2.1 Materials Limitations and Challenges

Although the materials that make the gas turbine engine have been optimized with cost considerations, limitations still exist. Steels and superalloys degrade due to the turbine engine environment. Steels tend to degrade from corrosion, oxidation, temper embrittlement, and graphitization [2]. Pitting corrosion and/or stress corrosion cracking are commonly found to be an issue in carbon steels and low alloy steels. Corrosion results in a loss of material and cracking. Likewise, carbon steels and low alloy steels are also

highly susceptible to oxidation. Therefore, at higher temperatures where oxidation is more prominent, stainless steel or superalloys are used.

Temper embrittlement occurs mostly in ferritic steels and some martensitic stainless steels. When the steel is exposed for a long period of time in the temperature range 350 °C – 550 °C, the material becomes brittle due to the presence of impurities [2]. This becomes a concern for parts that need good fracture properties, such as the rotor disks. To prevent embrittlement, it is vital that impurities such as sulfur, phosphorus and arsenic, are kept to a minimum in steels.

Another degradation mechanism that is prone to occur in iron or carbon steels is graphitization. During graphitization, carbon comes out and tends to migrate to the grain boundaries, forming graphite nodules in the iron or steel [2]. When steel or iron is exposed for long periods of time under temperatures above 400 °C, graphitization tends to occur, thus weakening the material and increasing the chances of crack propagation.

Although Ni-based superalloys are great creep resistant materials, they are still susceptible to oxidation at temperatures above 950 °C. Because the Ni-based superalloys are used in the high temperature parts of the engine, thermal cycling and shock are issues where stress build-up in the component will occur due to the presence of thermal strain [12]. The constant presence of strain could lead the material to undergo stress relaxation and deformation under creep. On the other hand, as the engine shuts down and the component cools, the Ni-based superalloy may not be able to relax, thus high residual stresses may result [2, 12]. These residual stresses would initiate cracks that grow to a

critical size, leading to catastrophic failures. With careful consideration when designing the components, the above degradation mechanisms can be avoided.

1.3 Materials Systems Overview

The durability and performance of the alloys and composite materials in the gas turbine engine increases when protective coatings are applied. Coating systems are a way to provide clearance control, wear resistance, and thermal and oxidation protection [2]. The fan and compressor parts are typically coated with wear and/or erosion resistant and abradable coatings. In combustor and turbine areas, TBCs and oxidation corrosion-resistant abradable seal systems are applied to the superalloys.

Abradable coatings are porous and applied as clearance coatings. The coating is designed to increase efficiency by minimizing gas leakage over the blade tips. In order for the coating to be effective, the porous nature allows the coating to be soft enough for the blade tip to cut a path into the abradable layer yet maintain the structural integrity and resist erosion from the gas stream [13]. Figure 2 below shows the typical microstructure of an abradable coating.

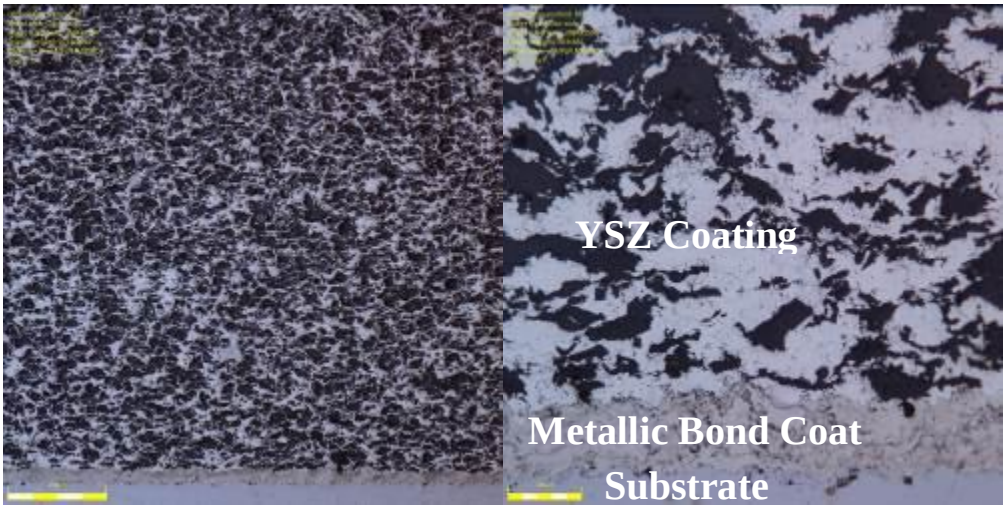

Figure 2: Microstructure of abradable coating with optical microscope: (a) 1.0x zoom (b) 1.5x zoom

Components in the compressor, combustion, and turbine areas often experience vibrations and dynamic forces that cause wear. Therefore, wear resistant coatings are used to prevent abrasive, erosive, and fretting degradation. This coating prolongs the life of the engine parts and consequently decreases the amount of maintenance required. Thermal and oxidation coatings help to increase the creep, oxidation, fatigue, and corrosion resistance [4]. This type of coating is what enhances the superalloys to its full potential and will be discussed in further detail in the next section.

1.3.1 Thermal Barrier Coatings

TBCs play an important role in enhancing the performance of insulating components such as gas turbine and aero-engine parts that operate at elevated temperatures [14]. The use of TBCs have been shown to increase the efficiency as well as durability of such parts. Due to their low thermal conductivity, when exposed to heat flow, the coating is able to bear a large temperature gradient. There are two different ways that the heat insulation property of TBCs can be utilized in components [15]. First, the service life of

the component can increase by keeping the working temperature of the engine unchanged and therefore the underlying substrate temperature decreases. Secondly, the efficiency can be improved by increasing the working temperature to a level at which the TBC insulates the substrate at constant temperature below the degradation temperature [15]. The most commonly used TBC system consists of an YSZ top coat and a metallic bond coat that is generally deposited on a Ni-based superalloy.

YSZ is most widely used because of its low thermal conductivity, high phase stability, high thermal expansion coefficient and high fracture toughness compared to many other ceramics [16]. Typically, the YSZ top coat is approximately 100-300 μm thick allowing a temperature drop up to 170°C between the top coat surface and substrate [16]. This drop in temperature provides many advantages as some were previously mentioned, but another advantage to the reduction in temperature is the reduction in the resulting creep [15]. Figure 3 below shows a schematic of the TBC layers and where the coating would be applied on turbine blades in aero-engines.

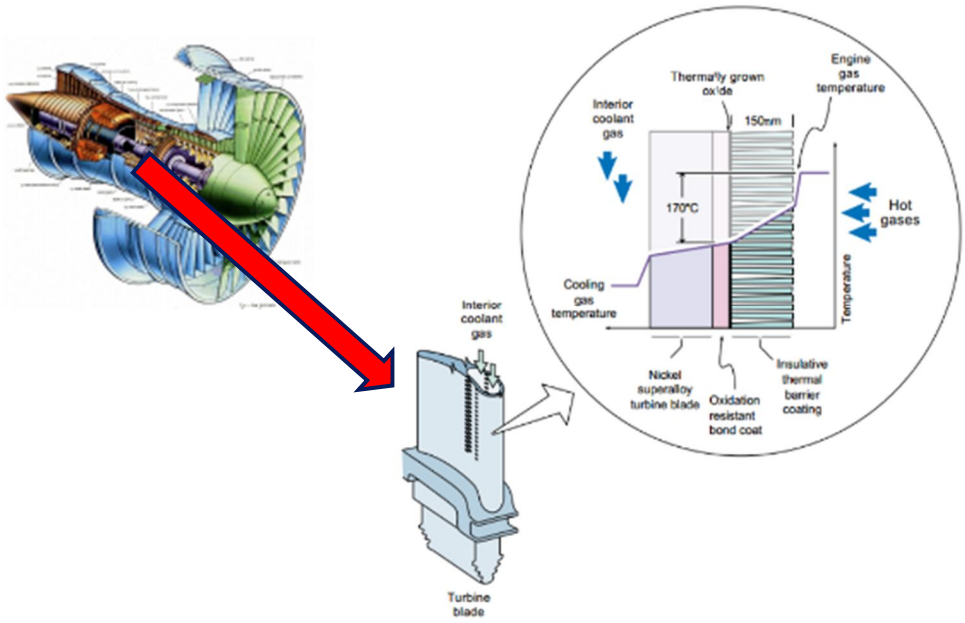

Figure 3: Schematic of TBC system on a turbine blade as a component of jet engine [15, 17], Schematics have been released by A. Karaoglanli, K. Ogawa, A. Turk, and I. Ozdemir, "Thermal Shock and Cycling Behavior of Thermal Barrier Coatings (TBCs) Used in Gas Turbines." *InTech*. [online] 2014, Chapter 10, pp 237-260 and D.D. Hass, "Thermal barrier coatings via directed vapor deposition," *Department of Materials Science and Engineering, Vol. PhD. Charlottesville, VA: University of Virginia*, [online] 2001, pp 1-256 into public domain, 2015

The substrate material is the main element that needs to be protected. Ni-based superalloys are generally used because of their ability to retain its strength at high temperatures (~1100°C) [18]. The substrate is typically produced with a directional grain or single crystal structure in order to increase the high temperature creep resistance [18]. Although the working temperatures of superalloys are high, in the range of 1050 °C to 1200 °C, coatings are able to increase the work temperatures even higher up to 1600 °C [6] and to extend the service life of the components especially after the rapid temperature changes the parts undergo during thermal cycling.

The coating between the substrate and the ceramic coating is multifunctional. This bond coat is typically made of a (Ni, Co) CrAlY alloy [19]. The coating provides a suitable thermal expansion match between the top coat and the substrate as well as a protection to the substrate from rapid oxidation and corrosion. At elevated temperatures, oxygen transfers from the top coat to the bond coat thus forming a thermally grown oxide (TGO) layer. This layer is desired to consist of a homogenously distributed and dense α-Al_2O_3 [12]. The reason for wanting the TGO layer to consist of α-Al_2O_3 is the low oxygen permeability of this alumina phase. However, there will be various spinel and metallic oxides apart from alumina. Other oxides that are present include: Cr_2O_3, NiO, and (Ni, Co)$(Cr,Al)_2O_4$ [18]. Although this layer protects the substrate against further oxidation, the continued growth of TGO during thermal cycling may lead to failure of the YSZ layer [2, 16].

1.3.2 Atmospheric Plasma Spray Process

TBCs are typically applied using atmospheric plasma spray (APS) process although electron beam physical vapor deposition (EB-PVD) is used as well. APS and EB-PVD coatings result in distinct microstructural differences, producing laminar and columnar structures respectively [20]. The columnar structure deposited from EB-PVD is less effective in hindering thermal heat transfer, however there is enhancement in the strength of the coating adhesion and improvement in strain resistance [20-21]. Compared to APS, EB-PVD has a higher erosion resistance and a smoother surface finish [21]. The smooth surface finish has an advantage aerodynamically in the reduction of friction and drag to improve efficiency and fuel cost [22]. Although EB-PVD coatings have excellent

characteristics, the process is complex, expensive, and there are difficulties in the utilization of raw materials with complex compositions such as (Ni, Co) CrAlY. For these reasons, the APS process is still commercially preferred. The APS process schematic is shown in Figure 4 below.

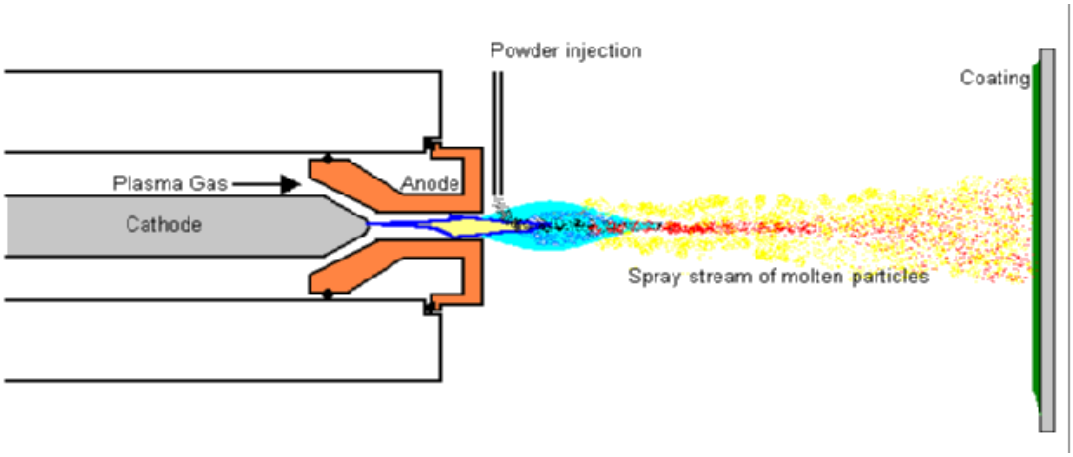

Figure 4: Schematic of air plasma spray process [23], Schematic has been released by "Plasma spray process," *Gordan England*, [online]. http://www.gordonengland.co.uk/ps.htm into public domain, 2015

As seen in Figure 4 above, molten particles are deposited on a substrate forming splats and layer by layer form the coating [23-24]. The material of choice for the TBC usually comes in powder form and is injected into a high temperature plasma flame. The powder is then rapidly heated and accelerated at a high velocity that upon impact, forms a mechanical bond with the surface. The build-up of the succeeding particles results in the final thickness of the TBC [24]. However, not all particles achieve the same velocity and temperature and consequently, the particles are not guaranteed to be the same size [25]. A model of the TBC structure sprayed by APS can be seen in Figure 5 below.

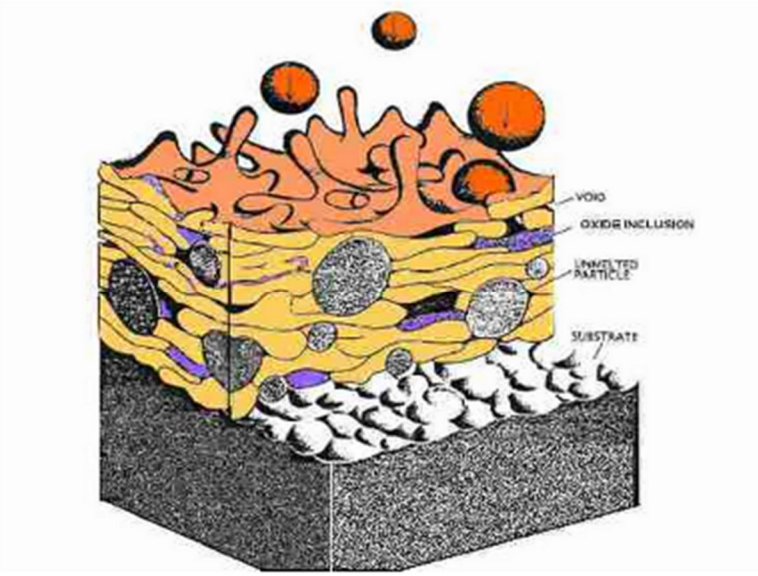

Figure 5: Schematic of thermal spray coating [25], Schematic has been released by "Thermal Spray Coatings," Gordan England, [online]. http://www.gordonengland.co.uk/tsc.htm into public domain, 2015

As mentioned earlier, APS coatings exhibit a lamellar grain structure resulting in an anisotropic behavior. APS coatings have distinctive defects such as voids, cracks, unmelted particles, and oxide formations. Having voids present is beneficial as it helps reduce stress levels and increases the shock resistance of the coating.

Cracks occur due to the rapid cooling of the particles. Micro-cracks can help alleviate some stress, but there is a tendency for the micro-cracks to transition to large macro-scale cracking. This becomes an issue in delamination and ultimately coating failures. Unmelted particles are outcomes from the differences in velocity and spray angle. Under stress or other physical factors, these globular particles have a tendency to behave isotropically, which in the anisotropic structure of the coating, acts as secondary defects which degrades the functionality of TBCs [26].

Because the APS process is performed in ambient environments, the coatings often have oxides embedded in the particle layers. Although the presence of oxides allows the coatings to be more wear resistant, the oxides can also lead to degradation from corrosion, reduction in strength and machinability of the sample [25].

1.4 Sample Preparation and Characterization

The key quality metrics for TBCs are the layer thickness, percent porosity in the ceramic layer, and other defects including cracking and oxidation of the metallic layer. In order to characterize TBCs, a cross-sectional, destructive analysis such as metallography is used to ensure quality from supplier qualification and quality assurance in production. Accurate evaluation of the microstructure of TBCs is essential to prevent turbine engine failures that could lead to catastrophic events.

Metallography is the study of a material's microstructure. Generally, sample preparation includes: sectioning, mounting, grinding, polishing, and then optical characterization. However, because of the brittle and porous nature, TBCs are one of the most challenging systems for metallographers. Sectioning of the substrate is typically done with the sample under compression using a precision saw to obtain a cross section of the sample. Mounting is typically done with a two-part low viscosity epoxy resin. The purpose of the mounting step is to protect the sample edge and integrity of the surface features. The epoxy impregnates the pores in the TBCs for protection and allows for easy handling of the sample during the next phase of grinding. Once cured, the sample is usually ground with silicon carbide (SiC) paper to remove damage created from sectioning. After

grinding, the sample is polished to remove damages caused from the cutting and grinding stages. At the end, the sample should have a mirror like finish. Finally, with optical microscopy, the sample images can be captured and the thickness and percent porosity measured. There have been suggested best practices, but variability still remains, causing an issue with supplier qualification and quality assurance, seen in Figure 6 below.

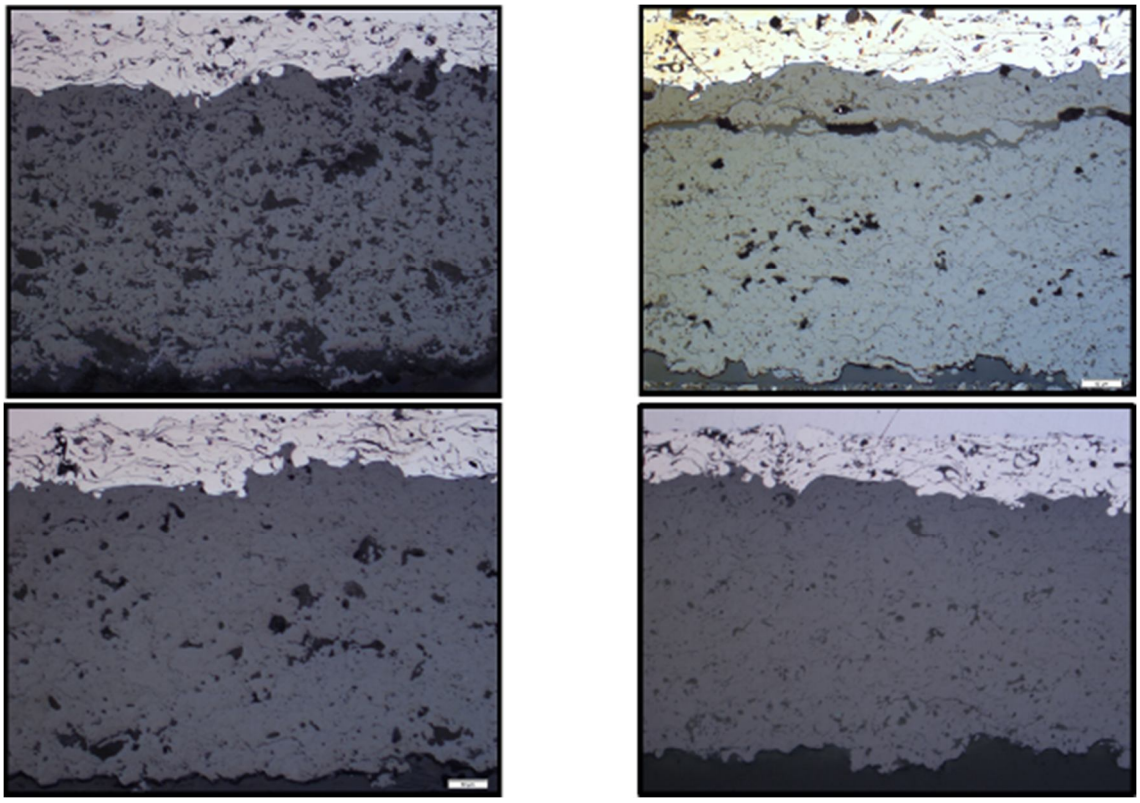

Figure 6: Microstructures of TBC that were sprayed under the same conditions

In collaboration with the CCAM, the samples in Figure 6 above were sprayed under the same parameters but with variations in the metallurgical procedures. However, there were differences in the reported percent porosity measurements and noticeable differences in the microstructures. Figure 7 below shows a common problem seen after sample preparation of TBCs.

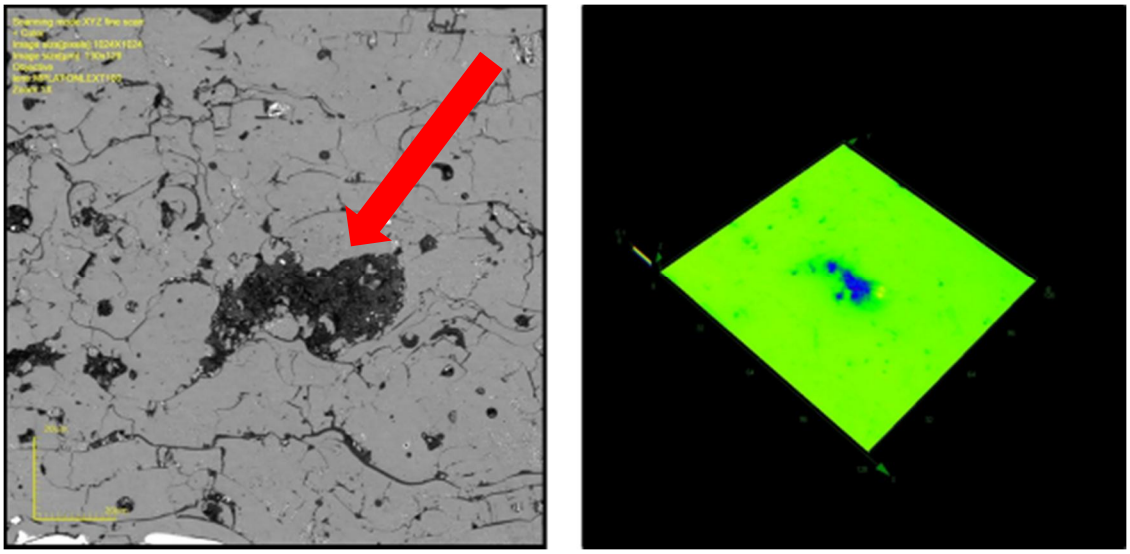

Figure 7: Microstructure of an oversized pore and 3D imaging using confocal microscope

A reoccurring issue with inconsistency in percent porosity measurements comes from the difficulty of differentiating filled pores and damaged, unfilled voids. As seen in Figure 7 above, what seems like an oversized pore, is in fact a pullout that was determined with the 3D imagining taken by a confocal microscope. Pullouts can be prevented with proper impregnation during the mounting process. This leads to the objective of this thesis.

1.5 Thesis Objectives and Overview

The goal of this research is to find and eliminate the variability during sample preparation. The reduction in variability in the sample preparation will allow for consistent and reliable characterization of the TBC microstructure. As mentioned previously, the epoxy impregnation of the pores is essential in protecting the sample edge and integrity of the surface features. Improved heating rates, curing kinetics of the epoxy could improve the impregnation properties. Therefore, the purpose of this research is to be able to determine whether or not the curing kinetics can be improved such that the

variability can be reduced. Understanding the curing kinetics could potentially prevent defects such as pull out of the coatings as well as a decrease in unpredictability during grinding and polishing. This will lead to the ability to accurately characterize TBCs and help supplier qualification and quality assurance of gas turbine engines for aircrafts.

2. Background

2.1 Crystal Structure of YSZ and α-Al_2O_3

YSZ typically make up TBC systems for previously mentioned reasons. Therefore, there needs to be an understanding of the crystal structure and physical properties of pure zirconium dioxide (ZrO_2) and why the addition of yttria (Y_2O_3) acts as a stabilization to the system.

Pure ZrO_2 is polymorphic, meaning that the material undergoes different crystalline modifications [27]. There are three possible crystal phases that exist for ZrO_2 at different temperatures. The crystal structures can be seen below in Figure 8 below.

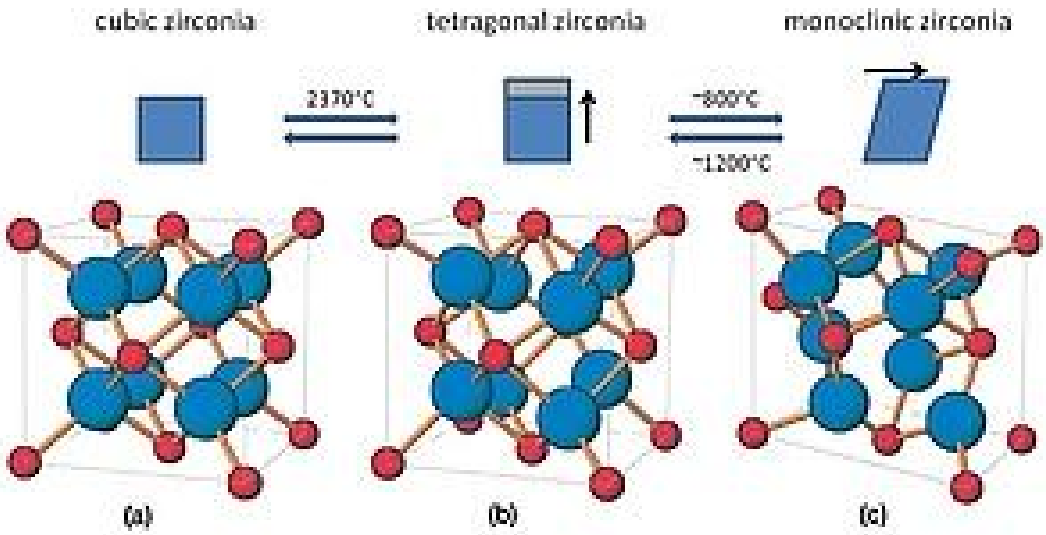

Figure 8: Schematic representation of the three crystal phases ZrO_2 undergoes [28], Schematic released by M. Hofmann, "Ageing behavior of 3Y-TZP dental ceramics in water, acetic acid and orthophosphoric acid at 80 °C," M.S. thesis, University of Tuebingen, Tubingen, Germany, [online] 2013. http://www.geo.uni-tuebingen.de/studium/studentische-projekte/wissenschaftliches-praesentieren-ss-2013-und-ws-201314/geowissenschaften/martin-hofmann.html into public domain, 2015

At high temperatures above 2370 °C, ZrO_2 exhibits a cubic structure. The cubic phase has a fluorite crystal structure where the Zr atom is coordinated by eight equidistant oxygen atoms. At temperatures between 1170 °C to 2370 °C, the material has a tetragonal structure. The tetragonal phase comes from the fluorite crystal structure, but the oxygen ions shift along one of the cubic axes and thereby elongating the structure. At temperatures, below 1170 °C, the material transforms from tetragonal to monoclinic. The monoclinic phase is a distortion of the cubic fluorite crystal structure [20].

As the ZrO_2 increases in temperature, the transformation from the monoclinic to tetragonal phase occurs rapidly and results in a 3% to 5% increase in volume. Extensive cracking occurs in the material due to the volume expansion which leads to failures in ZrO_2 components [30-31]. This causes concern when using pure ZrO_2 in components because of the spontaneous failure of its mechanical properties. When oxides such as Y_2O_3 are introduced, the temperature induced crystal phase structure changes significantly slows down [29]. Having the oxide present stabilizes ZrO_2 in the cubic crystal structure from its phase transition temperature down to room temperature [29]. This stabilize form of YSZ can be used for TBC systems.

As previously mentioned, the formation of α-Al_2O_3 is desired for the TGO layer. The α-Al_2O_3 structure is the irreversible, metastable structure of Al_2O_3 that forms initially with increasing temperatures. Crystallized sapphire or alumina (α-Al_2O_3) exhibits a corundum structure as shown in Figure 9 below.

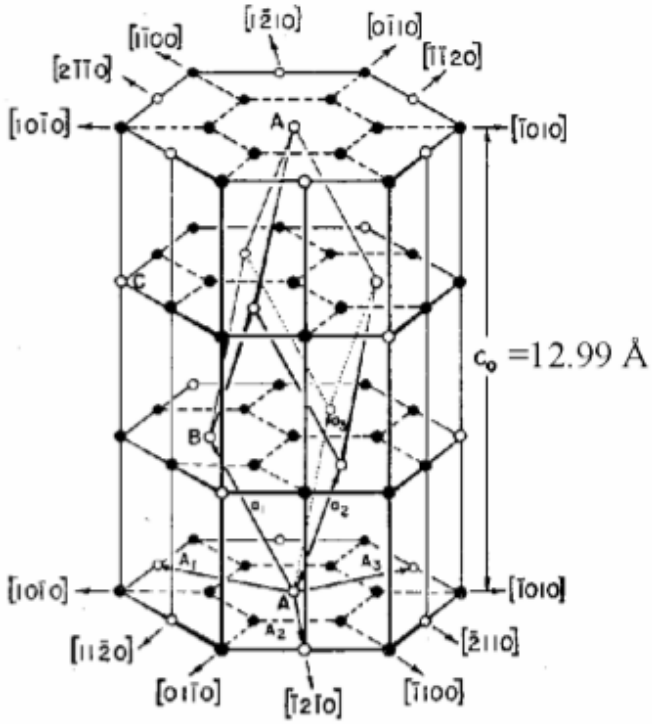

Figure 9: Crystal structure of sapphire [20], Schematic released by B. Rashkova, "Microstructural characterization of yttria-stabilized zirconia thermal barrier coatings grown on sapphire substrates," Ph.D. dissertation, University of Stuttgart, Stuttgart, Germany, 2003 into public domain, 2015

The oxygen anions (O^{2-}) form a hexagonal closed-packed (hcp) arrangement with the aluminum cations (Al^{3+}) occupying two-thirds of the octahedral sites [20, 27]. The maximum spacing of the Al^{3+} is achieved by building up similar layers. Alumina has excellent physical stability because of the strong chemical bonds between the Al and O ions. Because of the strong chemical bonds, α-Al_2O_3 has the highest hardness among oxides, has a high melting point, and high mechanical strength [20].

2.2 Thermodynamics of YSZ System

The crystalline phase of pure ZrO_2 is temperature dependent where the transformation back to the monoclinic from the tetragonal phase has proven to be detrimental for many applications using ZrO_2. However, by doping ZrO_2 with oxides such as Y_2O_3, the stability of the cubic and tetragonal phases is possible because doping increases the oxygen vacancy concentration and an enhancement of the oxygen ion conductivity. Important characteristics such as the thermal conductivity and fracture toughness depend on these phase and structural changes. The amount of Y_2O_3 effects the stability of the YSZ system and can be depicted with a phase diagram as seen in Figure 10 below.

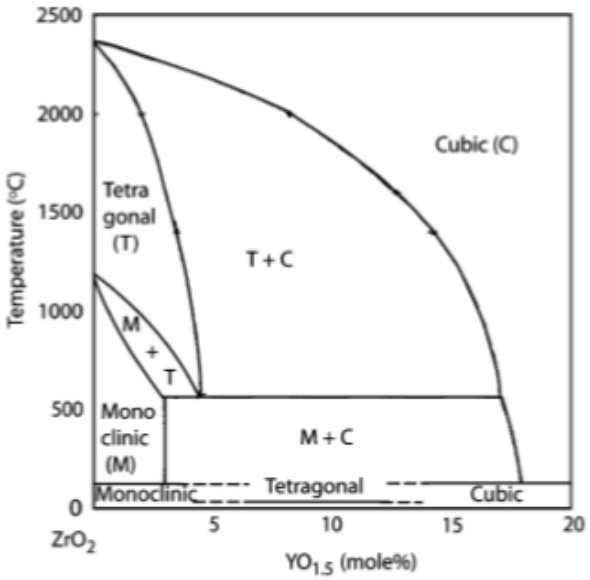

Figure 10: Phase diagram of $YSZ_{1.5}$ [30], Diagram released by G. Witz, V. Shklover, and W. Streurer, "Phase evolution in yttria-stabilized zirconia thermal barrier coatings studied by Rietveld refinement of X-Ray powder diffraction patterns," *The American Ceramic Society*, [online] 2007 into public domain, 2015

From Figure 10 above, the addition of 5-15 mol% yttria stabilizes zirconia at high temperatures in order to avoid the phase transitions that could lead to coating failures. TBCs are typically produced as a tetragonal metastable polymorph containing around 7-8

wt% yttria. At high cooling rates during the plasma spraying process, the 7-8 wt% of yttria results in a non-transformable tetragonal phase. This phase is how the addition of 7-8 wt% yttria gives the mechanical stability in YSZ coatings. Lower amounts of yttria results in a monoclinic polymorph that is only stable at lower temperatures. The transformation from monoclinic to tetragonal phase leads to an increase in volume which could instigate cracking and coating failures. Therefore, the monoclinic phase of YSZ is typically avoided in TBC coatings. On the other hand, higher yttria contents lead to a more stable cubic YSZ form at higher temperatures. This characteristic is ideal for the application of TBCs in aircraft engines.

2.3 Microstructure of YSZ grown by APS

There are different processes that are used to apply TBCs on a substrate. The most commonly used processes are APS or EBPVD. These processes result in different microstructures as seen in Figure 11 below.

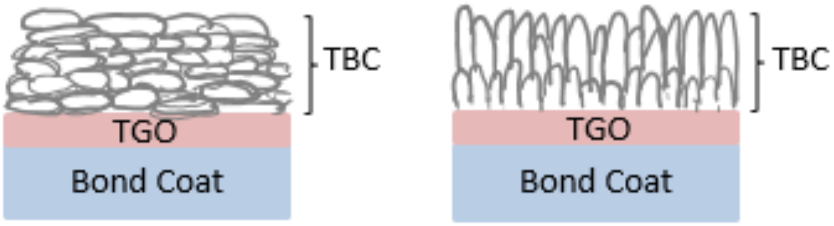

Figure 11: Schematic of TBC sprayed by APS and EBPVD respectively

APS is the preferred spray method because of the economical cost and the resulting laminar structure. This structure causes porosities and cracks to form parallel to the surface thus allowing a reduction in residual stress. The decrease in residual stress will decrease the thermal conductivity. The APS coatings have a thermal conductivity of 0.8-

1.0 W/mK at room temperature which is much lower compared to the thermal conductivity of EBPVD, which is 1.5-1.9 W/mK [22]. A lower thermal conductivity is the reason that APS coatings provide better thermal insulation during service.

During the APS process, the splats build up to create the coating. The microstructure of APS coatings depend on many spraying process parameters. One of the most important parameters that influences the microstructure of the coating is the substrate surface temperature [24]. Splats tend to be more loosely bonded on relatively low substrate surface temperatures (< 500 °C) forming micro-cracks [31]. The formation of the micro-cracks results from the temperature drop between the liquid phase of the splat and the surface temperature which introduces tension within the particle as seen in Figure 12 below.

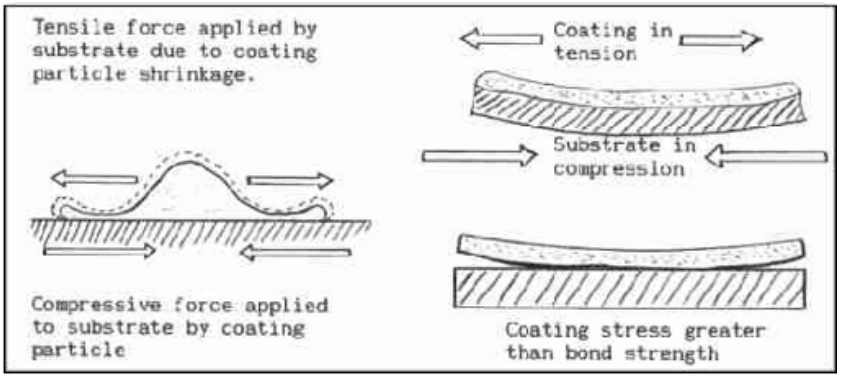

Figure 12: Schematic of the tensile stress in particle and compressive stress in the surface of substrate [25], Schematic released by "Thermal Spray Coatings," Gordan England, [online]. http://www.gordonengland.co.uk/tsc.htm into public domain, 2015

When the surface temperature of the substrate is low, the individually grown cracks in the splats do not connect with other splats which consequently creates possible paths for further crack growth under temperature loads. Conversely, when the substrate surface temperature is high during deposition, the splats tend to have a much greater bond with

each other due to diffusion and results in larger grain sizes [31]. With larger grains, the amount of grain boundaries decreases [31]. When the splat deposition on high surface temperatures cools rapidly to room temperature, compressive strain enables and supports the formation of cracks. The formation of cracks in the coating has advantages in thermal shock performances and the enhancement in strain tolerances.

Once the APS process is completed, as the substrate is cooled, transformation of the YSZ phases may occur. This will lead to a change in the original porosity content as seen in Witz [30] where after plasma spraying the porosity content was 17%-21%. However upon cooling, as the transformation from tetragonal to monoclinic YSZ occurred, the porosity content decreased to 12%-18% [30]. Due to the anisotropic behavior of the TBC, true percent porosity during characterization has been proven to be difficult.

2.4 Effect of Sample Preparation on Measured Porosity

From the preliminary investigation mentioned in Section 1.4, differences in metallurgical sample preparation led to inconsistent porosity measurements and noticeable differences in microstructures. Due to the variation in methods of preparation and characterization, there is generally no consensus amongst companies, mainly because suppliers deem their consumables as being necessary.

In a study done by Smith [32], three different grinding and polishing media were compared for the characterization of three common types of thermal sprayed coatings. The metallographic protocol of the media were SiC papers, bonded diamond platens, and

diamond slurries. Prior to grinding and polishing, the samples were sprayed under the same conditions, sectioned with a low speed diamond saw, and mounted in a two part epoxy. The samples and epoxy were preheated prior to mounting at 85 °C. Then the epoxy was mixed and evacuated in a bell jar at 130 to 400 Pa for one minute and was poured into the mount in air at room temperature. The mounts were then again evacuated for an additional minute and finally cured at 85 °C for 8 hours. Grinding and polishing were then carried out under the three different protocols and the apparent microstructures from those methods were compared based on the micrographs, percent porosity, and micro-hardness. The result from this study done by Smith and group [32], show that SiC papers caused in edge rounding and substantial pull-out along with higher apparent porosity compared to the diamond platen and slurry. The diamond platens resulted in less edge rounding and fewer pull-out while the diamond slurries consistently were able to achieve the best results.

From a study of suggested practices by Elssner [33], vacuum impregnation was highly recommended to impregnate the sample with epoxy. However, according to Elssner [33], the samples and epoxy resin should be evacuated at a pressure of 1000 Pa to 1500 Pa. The impregnation is done under vacuum and is performed by pouring the resin over the sample and evacuated for 10 to 30 minutes. This vacuum procedure varies greatly from the study done by Smith [32]. Grinding was done with a 20 μm diamond disk followed by a 10 μm diamond film. Polishing was completed by usage of diamond suspension on synthetic fiber cloth and nylon cloth with an alcohol-based or water-based lubricant. Each step during grinding and polishing was captured to show the final pore structure.

Brindley [34] brought awareness of the inconsistency in interpretation of TBC structures. The sample preparation in this study was different from the previous in that Brindley [34] vacuum mounted the samples prior to sectioning. After sectioning, the samples were mounted again and then ground with a 150 grit Al_2O_3 grinding stone before following a nine step polishing procedure provided by NASA. Grinding was completed on SiC paper and polishing was completed on a diamond synthetic hard cloth and completed on SiO_2 synthetic chemical resistant cloth. Brindley [34] points out the difficulties with distinguishing unfilled pores and epoxy filled pores from optical microscopy which makes it difficult to distinguish between interconnected porosity and pullout porosity. Therefore, Brindley [34] concluded that this technique to prepare porous and translucent TBC samples has an advantage over existing methods because of its ability to distinguish between interconnected porosity and pullout porosity.

Other studies done by Kelly [35], Voort [36], and Friel [37] have emphasized the use of a low viscosity epoxy to infiltrate the pores of TBCs. Although these studies have mentioned vacuum impregnation being ideal, the procedure is undefined. Furthermore, the grinding and polishing methods vary in paper type, cloth type, time, and pressure. As seen from these studies, there are a wide variety of ways to prepare TBC samples. Therefore, reducing inconsistency in the sample preparation is vital and begins with proper sectioning and mounting. The use of epoxy resins have been recognized as effective in protecting the integrity of the TBC structure, however, there are complications in the ability to thoroughly impregnate the pores. Shrinkage during curing could lead to surface distortion, internal cracks, and voids if not controlled.

2.5 Epoxy Resin Applications

Standard methodology for sample preparation of TBCs varies from company to company. Amongst each step in the process, variability has become a problem in the final characterization of the samples. Therefore, there is a need to understand and eliminate the cause of inconsistency by determining what variables matter in the sectioning and mounting process.

Epoxy resins are used in a variety of applications such as paints and coatings, adhesives, electrical insulators, and resin matrices for composite materials. Recently, advanced composite materials (ACMs) are being increasingly utilized in aerospace industry such as a composite wing. Hence the push for new manufacturing technologies to produce ACMs to be cost effective and efficient, given rise to the attention of resin film infusion (RFI) from textile preforms [38]. RFI process may be able to cost effectively produce strong yet light aerospace structures. The resin comes in a pre-cured film that is placed in a mold together with the dry fiber reinforcement. In order for the resin to impregnate the preform, heat and pressure are applied under conventional vacuum then followed by a cure. In one study done by Garchke [38], the goal was to be able to optimize the cure cycle while minimizing the processing time of the RFI process and understand how rheology of the resin film will be affected by faster processing methods. From the curing kinetics and viscosity model used to describe the chemo-rheological behavior of the resin film, Garchke [38] was able to investigate the effect of heating rates on the viscosity of the resin. From this preliminary investigation, as heating rates increased, the impregnation properties of the resin improved with a faster processing time. The gel time

shortens with the increase in heating rate, however, at ramp rates above 8 °C/min there seemed to be no more significant influence on further lowering the viscosity [38]. Therefore, in this study, it is believed that increasing heating rates from 1 °C/min to °6 C/min will narrow the processing window from 150 to 100 minutes as well as improving the impregnation properties of the film in the RFI process [38].

In another study by Garchke [39], there was a need to be able to cure composite parts without high pressure which is typically done in an autoclave. To eliminate the use of autoclaves would be a reduction in cure cycle time as well as overall costs. In this study, the flow behavior of the resin was studied which includes the heating rates and dwell times. Results from the experimentation showed that for out-of-autoclave cure cycles, when the dwell time shortened with a higher heating rate, the flow properties were improved and as a result toughening the resin system [39].

Other studies on fabrication of fiber-reinforced composites have focused on the curing kinetics of epoxy resin films or two part epoxies studied by Lee [40], Yang [41], and Jagadeesh [42]. Importance of the heating rate and temperatures have been emphasized in these studies and should be applied to understand whether or not the curing kinetics of a two part epoxy has a significant effect on the characterization of TBCs.

2.6 Epoxy Resins and Curing Agents

Two part epoxies consist of an epoxy resin and the epoxy curing agent that is sometimes referred to as the hardener. Epoxy resins are typically low molecular weight,

thermosetting polymers that contain one or more epoxide groups [43]. At higher molecular weights, the epoxy becomes more viscous. An uncured epoxy resin can react with many curing agents that contain hydroxyl, carboxyl, amine and anhydrides [43-45]. There are many uses for epoxy resins as they can be produced to have excellent adhesion, chemical resistance, low shrinkage, and sufficient mechanical properties. These characteristics are attractive to many industries such as construction, packaging, medical, and aerospace [43].

The most commonly used epoxy resin comes from the reaction of bisphenol A (bis-A) and epichlorohydrin [45]. Bis-A is carbon-based and is synthesized by the condensation of acetone with phenol [44-45]. The chemical structure can be seen in Figure 13 below.

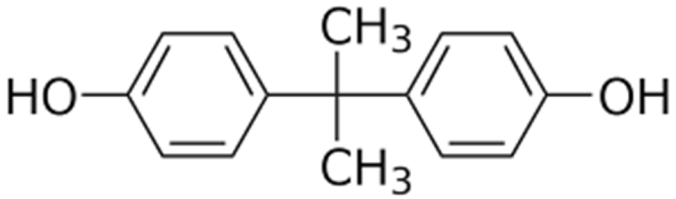

Figure 13: Chemical structure of bis-A [46], Schematic released by "Bisphenol A," *Wikipedia*, [online] 2006. http://commons.wikimedia.org/wiki/File:Bisphenol_A.svg into public domain, 2015

Bisphenol F (bis-F) is another commonly used compound in epoxy resins as it has a lower viscosity and a higher chemical resistance compared to bis-A [45]. The chemical structure can be seen in Figure 14 below.

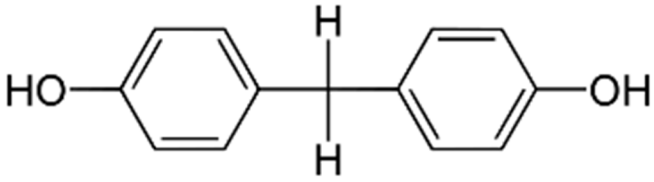

Figure 14: Chemical structure of bis-F [47], Schematic released by "Bisphenol F," *Wikipedia*, [online] 2006. http://en.wikipedia.org/wiki/Bisphenol#/media/File:Bisphenol_F.svg into public domain, 2015

Curing occurs when the linear structure of the epoxy resin forms a three dimensional cross-linked structure. This formation for a two part epoxy is done by reacting the epoxy resin with the hardener. The curing process relies heavily on the properties of the curing agents. The curing reaction, reaction rate, gel time, degree of cure, viscosity, curing cycle, and final properties are dependent on the hardener [43-45]. There are three main groups of curing agents: active hydrogen compounds, anionic and cationic initiators, and reactive cross-linkers [44].

Active hydrogen compounds include amines, amides, hydroxyls, and anhydrides. These reactive hydrogen compounds react by addition polymerization with the epoxide groups of the resin thus creating cross-links and a thermoset polymer. Amines and amides are most commonly used in industries. Amines are a result of when one or more hydrogens in ammonia are replaced by an organic alkyl or aryl group [45]. As a reactant agent, amines react with the epoxide group resulting in the formation of a hydroxyl group and a secondary amine, ether, or ester. The secondary amine can further react with an epoxide to form a tertiary amine and an additional hydroxyl group [44-45]. Amides are a result from the replacement of hydrogen with carbon or oxygen and an organic group in ammonia.

Compared to amines, amides are less durable and chemical resistant thus amines are more practical agents to use. However, amines and amides are highly reactive compared to hydroxyls and anhydrides [47]. Hydroxyls and anhydrides require a higher cure temperature as well as a longer cure time. Therefore, they are not as commonly used as curing agents in industry.

Anionic and cationic initiators act as catalysts for epoxy resins that are able to homopolymerize [44-45]. This means that in the presence of an anionic or a cationic catalyst, the resin is able to react with itself to form a cured structure. The cured network consists of ether bridges and exhibits high thermal and chemical resistance. However, this type of curing involves longer and higher curing cycles with poor cured properties such as brittleness [47].

Lastly, the reactive cross-linkers such as phenol, melamine, and formaldehyde resins are mainly used as surface coatings and films [46]. These type of curing agents have higher equivalent weights compared to the other two types of curing agents and cross-link with the second hydroxyls of epoxy resins or by self-condensation. Reactive cross-linkers are not typically used compared to amines because of the need to cure at high temperatures.

In this study, the epoxy resin from Buehler is a mixture of bis-A, bis-F, and alkyl glycidyl ether and is reacted with the curing agent isophorone diamine. Bis-A as mentioned earlier is a commonly used epoxy resin as well as bis-F. Alkyl glycidyl ether is a reactant of the

bis-A and epichlorohydrin [48] and acts as a reactive diluent thus lowering the viscosity of the epoxy resin [47]. Isophorone diamine is an organic compound with multiple amino groups with a chemical structure as seen in Figure 15 below [49].

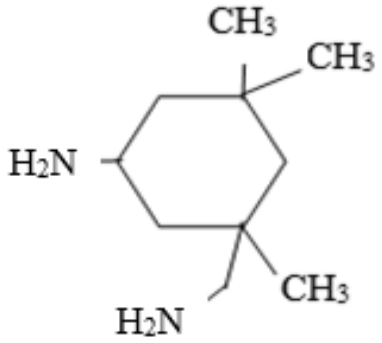

Figure 15: Chemical structure of isophorone diamine

Isophorone diamine is a cycloaliphatic meaning that it exhibits a ring structure which allows more of a flexible structure compared to a linear chain created from other curing agents. This flexible structure allows for better toughness of the epoxy [50]. The curing reactions between the resin and hardener will be discussed further in the next section.

2.6.1 Curing Reactions

As the epoxide is mixed with a curing agent or a catalyst, there is a transformation from low molecular weight to a cross-linked structure. Oxygen has a high electronegativity forming a polar bond with the carbon atoms [44]. The epoxide rings are unstable and can be easily broken by the curing agent. As the epoxide rings open up, hydroxyls (-OH) form which continues to react and crosslink with the curing agents [48]. The chemical structure of bis-A diglycidyl ether can be seen in Figure 16 below.

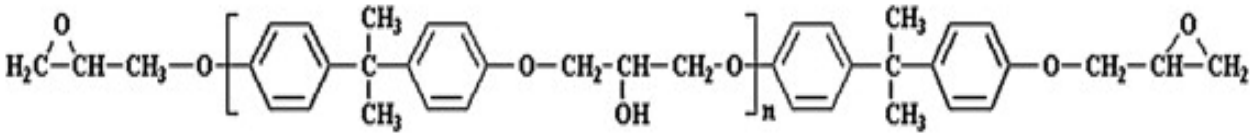

Figure 16: Chemical structure of Bis-A diglycidyl ether [48], Reprinted from J. Abenojar, N. Encinas, J.C. del Real, and M.A. Martinez, "Polymerization kinetics of boron carbide/epoxy composites," *Thermochimica Acta Elsevier*, [online] 2014, with permission from Elsevier

During the polymerization reaction, -OH groups are generated and act as catalysts thus increasing the initial reaction rate and the curing reaction repeats itself with the addition of more molecules. A general cure reaction can be seen in Figure 17 below.

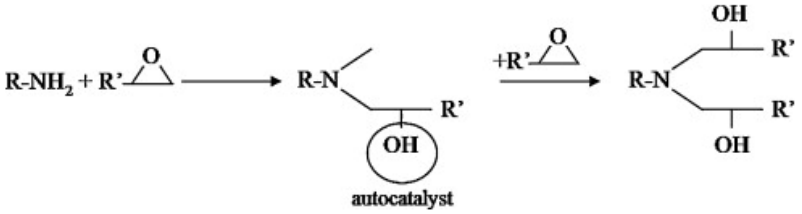

Figure 17: General cure reaction by polyaddition with active hydrogen atoms [48], Reprinted from J. Abenojar, N. Encinas, J.C. del Real, and M.A. Martinez, "Polymerization kinetics of boron carbide/epoxy composites," *Thermochimica Acta Elsevier*, [online] 2014, with permission from Elsevier

As more molecules are being added, the molecular weight increases and finally creating a three-dimensional structure.

2.6.2 Curing Analysis Techniques

The curing process of epoxy resins can be studied either by chemical and/or physical methods. Some chemical based techniques include Fourier transform infrared spectroscopy (FTIR), nuclear magnetic resonance (NMR), high performance liquid chromatography (HPLC), and radiochemical methods [44]. Some physical based

techniques include thermal gravimetric analysis (TGA), differential scanning calorimetry (DSC), thermal scanning rheometry (TSR), thermomechanical analyzer (TMA) and dynamical mechanical analyzer (DMA) [44]. Two different methods can sometimes be used together in order to understand the curing mechanisms and to determine the kinetic parameters for modeling.

2.6.3 TGA

TGA is a thermal analysis technique that measures the change in weight of a material as a function of temperature or time in a controlled atmosphere [51]. This technique is useful for studying inorganic materials, metals, ceramics, glass, composites, and especially polymeric materials such as thermoplastics, thermosets, elastomers, plastic films, coatings, etc [51-52]. Information about the materials physical and chemical phenomena can be determined from the TGA. Measurements on the thermal and oxidative stabilities, lifetime, decomposition kinetics, moisture and volatile contents, and how the material reacts to the atmosphere are some of the information that can be provided [51]. The TGA system can be seen in Figure 18 below.

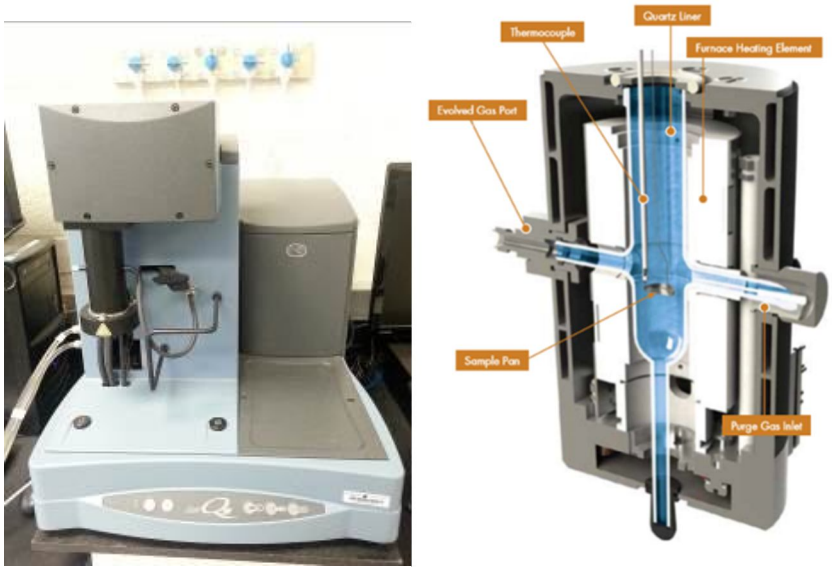

Figure 18: Q50 TGA system and cross section schematic from TA Instruments [53], Schematic released by "Thermogravimetric analysis," *Wikipedia*, [online] 2015. http://en.wikipedia.org/wiki/Thermogravimetric_analysis into public domain, 2015

The TGA system consists of precision balance that supports the sample pan with a thermocouple adjacent to the pan. The thermocouple allows for accurate temperature measurements by comparing the voltage output with the table of voltage versus temperature provided in the software [51]. Programming the furnace to run at a constant heating rate or heating to obtain a constant mass loss with time is possible. Some furnaces are lined with quartz which is chemically inert to the decomposition products of a particular sample and is resistant to the adsorption of off-gas products [53]. The lining reduces the internal volume which allows those products to rapidly leave the chamber meaning a more precise measurement. In order to prevent oxidation or other unwanted reactions, a sample purge gas flows directly across the sample and exits through an exhaust thus controlling the sample environment [53]. The mass of the sample is observed throughout the experiment and plotted with mass loss as a function of temperature or time [51-53].

With increasing temperature, the components of the sample will begin to decompose. As a result of the decomposition, a mass change in the sample will occur. The weight percentage of the mass change can be measured and plotted for analysis. TGA can be used to evaluate thermal stability of a material. If a material is thermally stable, there will be no noticeable sample mass loss. TGA is also able to determine the maximum temperature of a material before degradation. As temperature increases, the material may lose mass through chemical reactions, the release of adsorbed species, and decomposition. When either of these events occurs, the material is no longer thermally stable and can be seen on the plot by a significant drop in slope. TGA can provide complimentary and supplementary characterization information to DSC, another thermal analysis technique.

2.6.4 DSC

DSC is another widely used thermal analysis technique to characterize the properties of polymers [54]. These properties include but are not limited to the glass transition temperature, melting temperature, and crystallization. The DSC system can be seen in Figure 19 below.

Figure 19: Q20 TA Instrument DSC system

A reference pan and a sample pan are each placed on two thermocouples in the DSC system. Dynamic DSC where a specific heating rate can be specified or an isothermal DSC where the temperature is held constant for a certain amount of time can be used to gain different information about the polymer [55]. At a specified ramp or temperature hold, the DSC determines the difference in the amount of heat required to increase the temperature of a sample and reference measurement as a function of temperature [55-56].

This technique uses the principle that a sample will undergo a phase transition as more or less heat flows through the sample than the reference. The amount of heat flow depends on whether the nature of the sample will go through an exothermic or an endothermic reaction. For example, when a solid sample melts to a liquid, there is a greater amount of heat flow required in order to increase its temperature at the same rate as the reference. This reaction is an endothermic process since the sample absorbs the heat. On the other hand, when the sample goes through an exothermic process, less heat is required to

increase the sample temperature. The amount of heat absorbed or released during the phase transitions can be measured by the DSC and a heating or cooling curve is created.

The enthalpy of the transition can be calculated from the curve by integrating the corresponding peak and can be expressed by the equation [56]:

$$\Delta H = kA \quad (1)$$

where ΔH is the enthalpy of transition, k is the calorimetric constant, and A is the area under the curve. Instruments with complimentary software packages are able to calculate this change in enthalpy.

3. Experimental

3.1 Materials and Methods

The TBC samples were sprayed by the APS process and provided by the CCAM. EpoHeat-2 is a Buehler product and is a slow cure two part epoxy resin used in this study. Buehler provided the information of viscosity for the mixed epoxy to be approximately 500 cps at room temperature. When heated at 55 °C, the viscosity decreases to approximately 34 cps. The low viscosity allows for better impregnation of pores in the TBC.

3.2 TGA Measurements

The TGA run was carried out on TA Instruments Q-Series: Q50-1415. A ratio of 100:21 by weight of the epoxy resin and hardener was mixed for two minutes until uniformly dispersed. The mixed epoxy resin was weighed out to be 39.95 mg in a platinum pan.

The sample was placed in a platinum pan and the weight loss was observed by the dynamic scan with a heating rate of 20 °C/min to 500 °C under a nitrogen purge flow of 50 ml/min. The temperature before degradation and amount of weight loss was determined from the data collected.

3.3 DSC Measurements

Both dynamic and isothermal DSC runs were carried out on TA Instruments Q-Series: Q20-2292. A volumetric ratio of 4:1 of the epoxy resin and hardener were mixed for two minutes until uniformly dispersed. Dynamic DSC was studied with and without heating

the epoxy resin prior to testing. Without heating, the epoxy resin and hardener was mixed for two minutes and placed in an aluminum cell. With heating, the epoxy resin and hardener was mixed for two minutes and then heated at 55 ℃ for 5 minutes. A small quantity of the sample (1-5 mg) was taken for DSC measurements in an aluminum cell. An identical empty cell was taken as reference.

A small quantity of the sample was sealed into an aluminum cell. The dynamic and isothermal scans were taken in a nitrogen atmosphere with a nitrogen purge flow of 50 mL/min to minimize oxidation of the sample during curing. For dynamic DSC, the samples were heated from 40 °C up to 300 ℃ at rates of 2 ℃/min, 5 ℃/min, and 10 ℃/min. For isothermal curing, the samples were measured at constant temperature of 50 ℃, 60 °C, 70 ℃ and 80 °C for 100 minutes. The exothermic reaction was considered complete when the signal reached a plateau. The final baseline was estimated to determine the heat of reaction under the exothermic curve and the heat of curing.

3.4 Sample Preparation for Metallography

3.4.1 Sectioning

The TBC 80 mm x 25 mm sample coupons provided by CCAM needed to be sectioned prior to mounting. Each sprayed coupon provided six samples. The coupons were transversely cut with a 20 HC diamond wafering blade on Buehler's IsoMet 4000 Linear Precision Saw. The sectioning parameters is shown in Table 1 below.

Table 1: Sectioning Parameters

Sectioning Parameters	
Blade Speed	2000 RPM
Feed Rate	1.2 mm/min
Distance Remaining	> 30 mm
Coolant	Water

The diamond blade was dressed prior to the section each sample coupon. Each sample coupon was able to produce six samples to mount. The median setting for the blade speed and the slow feed rate allows for minimal damage to the brittle ceramic coating. After sectioning, the samples were rinsed with water and soaked in isopropanol alcohol for five minutes then air dried at room temperature.

3.4.2 Mounting

Mounting is an important step to protect the sample edge and integrity of the TBC surface features. EpoHeat-2 is a two part, low viscosity epoxy by Buehler that was used to mount the samples. The epoxy curing temperature recommended by Buehler is 55 °C for 90 minutes. Buehler suggested to heat the epoxy mixture for five minutes prior to mounting in order to lower the viscosity even more thus improving the impregnation properties. From the DSC data that will be discussed in more detail later, 70 °C was determined to have the greatest cure reaction heat. Therefore the curing temperatures were set at 55 °C and 70 °C for a dwell time of two hours with ramp rates of 2 °C/min, 5 °C/min, and 10 °C/min. The experimental parameters are shown in Table 2 below.

Table 2: Experimental parameters for curing

Heating Rate, °C/min	Temperature, °C	Number of Samples
2	55	3
5	55	3
10	55	3
2	70	3
5	70	3
10	70	3
No Rate	55	3
No Rate	70	3

The same parameters are repeated but with heating the epoxy resin prior to filling the samples.

A volumetric ratio of 4:1 resin to hardener was used. While slowly mixing, the hardener was gradually poured into the resin with a total mixing time of approximately two minutes, or until the mixture was uniformly dispersed. For the set of runs that the epoxy was heated prior to impregnation, the mixture was placed on a hot plate set at 55 °C for five minutes. The epoxy was then poured into the sample cups and placed in a Barnstead/Thermolyne 1500 Furnace. Another thermocouple was placed in the furnace to monitor the temperature setting. At a fast heating rate of 10 °C/min to 70 °C, the furnace tends to overshoot to 95 °C. Therefore, the furnace door was opened and it took approximately 30 minutes to bring the furnace temperature back down to 70 °C. In order to decrease the amount of time it takes to equilibrate the furnace, the furnace door was opened when the temperature began to increase past 75 °C. The amount of time to decrease the temperature was then approximately 15 minutes. Although there is the

overshoot concern, based on the TGA data, no significant decomposition would occur. After two hours of curing, the samples were left in the furnace to slowly cool for five minutes before being taken out to cool at room temperature.

3.4.3 Grinding and Polishing

The grinding and polishing procedures closely simulated industry practices. With an automated Buehler AutoMet 2 Power Head and EcoMet 3, six samples could be ground and polished at the same time. The procedure is listed in Table 3 below.

Table 3: Grinding and Polishing Procedure

	Paper	Grit	Lubricant	Time, min	Speed, rpm	Force, lb
Initial Grind	SiC	120 P	Water	2	150	20
Grind	SiC	220 P	Water	2	150	20
		500 P	Water	2	150	20
		1200 P	Water	2	150	20
		2400 P	Water	2	150	20
Polish	Durasilk	9 µm	Diamond Suspension	6	150	20
	Durasilk	3 µm	Diamond Suspension	6	150	20
	Durasilk	1 µm	Diamond Suspension	3	150	20
	Chemicloth	0.05 µm	Alumina	1*	150	20

In between each grinding and polishing stage, the samples were rinsed with water. The last polishing step was done for thirty seconds of 0.05 µm alumina colloid followed by

thirty seconds of water. Once completed, the samples were rinsed with water and then ethanol and dried immediately.

4. Results and Discussion

4.1 TGA analysis

TGA analysis was performed in order to determine the maximum temperature before decomposition of the epoxy occurred. The final curve and analyses by TA Instruments Universal Analysis software of the epoxy resin is shown in Figure 20 below.

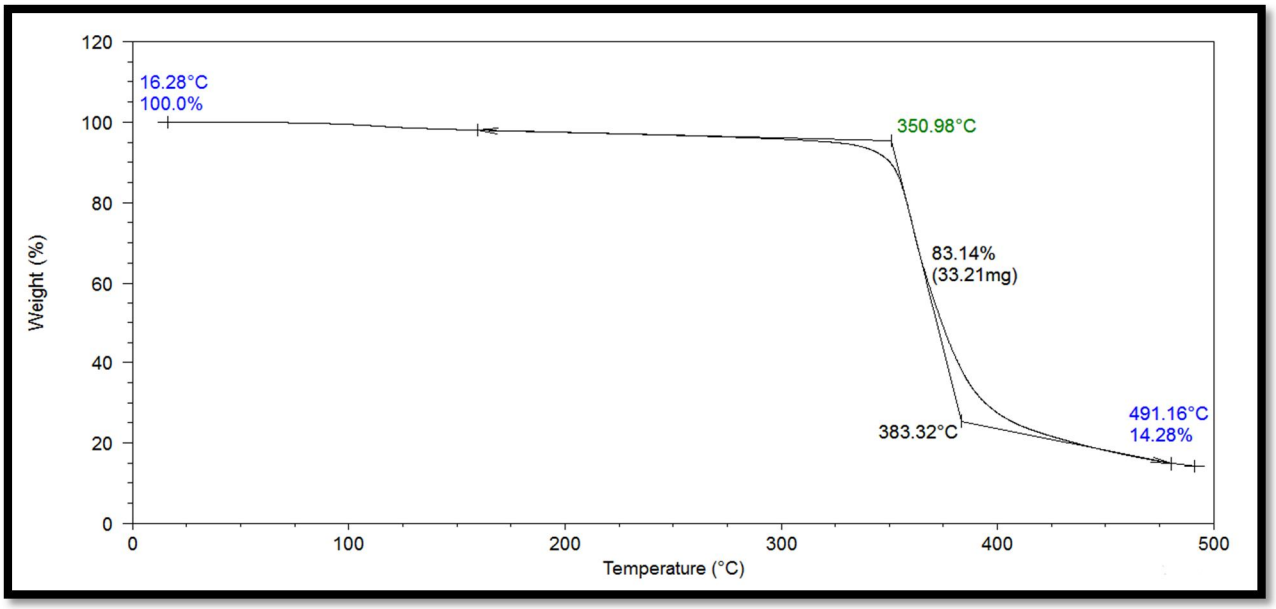

Figure 20: TGA curve for epoxy resin at 20 °C/min to 500 °C

At the start temperature of around 16.28 °C, there is 100 wt% of the epoxy resin. The onset temperature denotes when weight loss and decomposition to volatile products begins. Using the analytic tool in the TA Instruments Universal Anlysis software, decomposition began to occur at approximately 350.98 °C with a 2% weight loss. At the end of the run, a remainder of 14.28 wt% was left. With the TGA data, the maximum temperature for the dynamic DSC was determined to be 300 °C.

4.2 Dynamic and Isothermal DSC Analysis

From the TGA analysis, the temperature before the epoxy resin will decompose and volatize was determined to be about 300 °C. Therefore, the dynamic DSC was done at the specified heating rates up to 300 °C as seen in Figure 21 below.

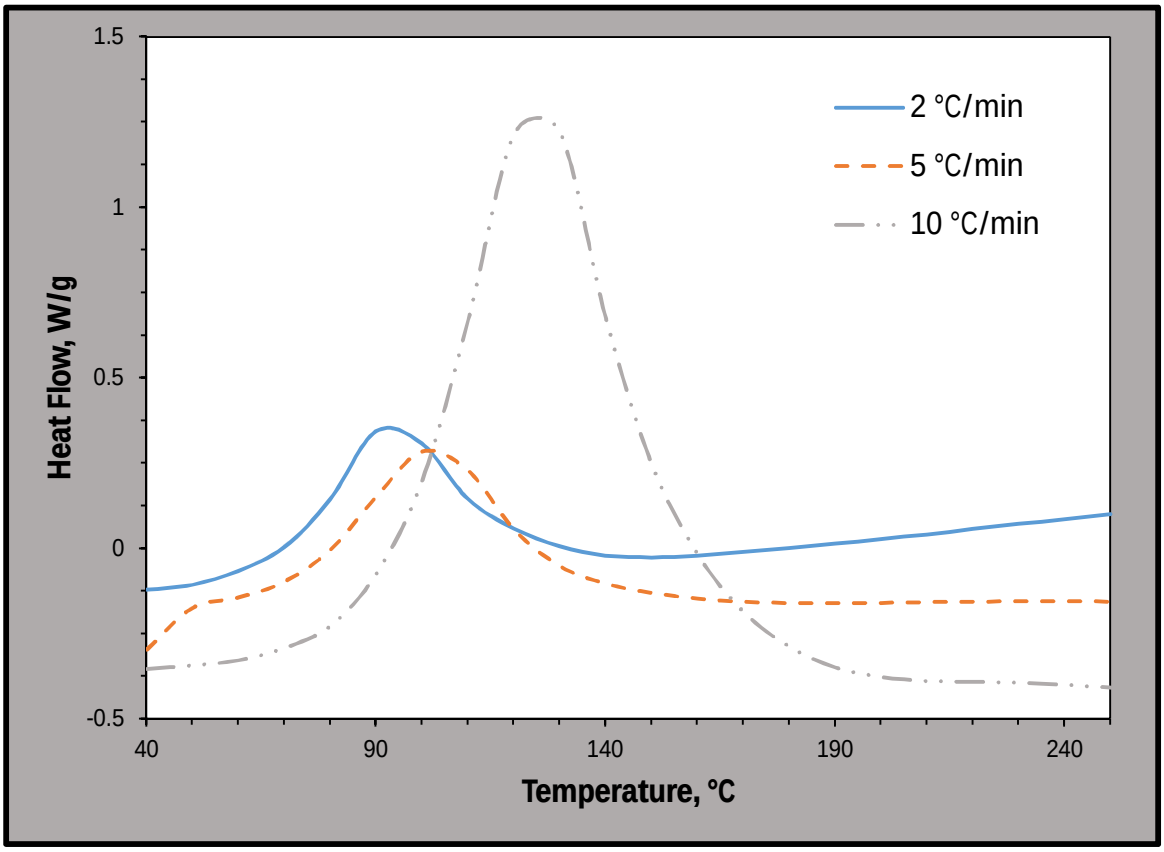

Figure 21: Dynamic DSC without heating epoxy resin at heating rates 2 °C/min, 5 °C/min, and 10 °C/min

Each heating rate was repeated five times for consistency. The higher the heating rate, the more rapidly heat flows into the system causing an increase in temperature which increases the heat capacity of the epoxy resin. Increasing the heating rate also means less time for the chemical groups to react. Therefore from Figure 21 above, the peak curing

temperatures, onset, and final temperature increased as the heating rate increased resulting in the shifting of the peaks.

By averaging the five runs, the peak curing temperature for 2 °C/min was 91.50 °C and the average onset temperature was 64.35 °C with a standard deviation of 2.66 and 3.82 respectively. For the heating rate of 5 °C/min, the average peak curing temperature was 108.00 °C and the average onset temperature was 75.12 °C with a standard deviation of 3.64 and 5.29 respectively. Finally the average peak cure temperature for 10 °C/min was 124.60 °C with an average onset temperature of 88.80 °C with a standard deviation of 2.34 and 3.59 repectively.

Table 4: Average Values for Dynamic DSC Peak Integration at Various Heating Rates

Average Peak Integration		
Heating Rate, °C/min	**Onset, °C**	**Peak T, °C**
2	64.35	91.50
5	75.12	108.03
10	88.80	124.60

There was a variation in the amount of heat released during each runs of the different rates. For the ramp rate of 2 °C/min, the range was from 77.50 J/g to 440.80 J/g. The heating rate of 5 °C/min gave a range of 50.56 J/g to 407.70 J/g. And lastly, the heating rate of 10 °C/min gave a range of 73.80 J/g to 460.00 J/g. The wide range could be due to a number of factors such as the ratios of the epoxy resin and how uniform the mixing was

done. The amount of time it took for the sample to be placed into the DSC instrument could also be a factor to the difference in the exothermic reactions.

When the epoxy resin was heated prior to the dynamic DSC runs, there was not much of a difference in the peak curing temperatures as seen in Figure 22 below.

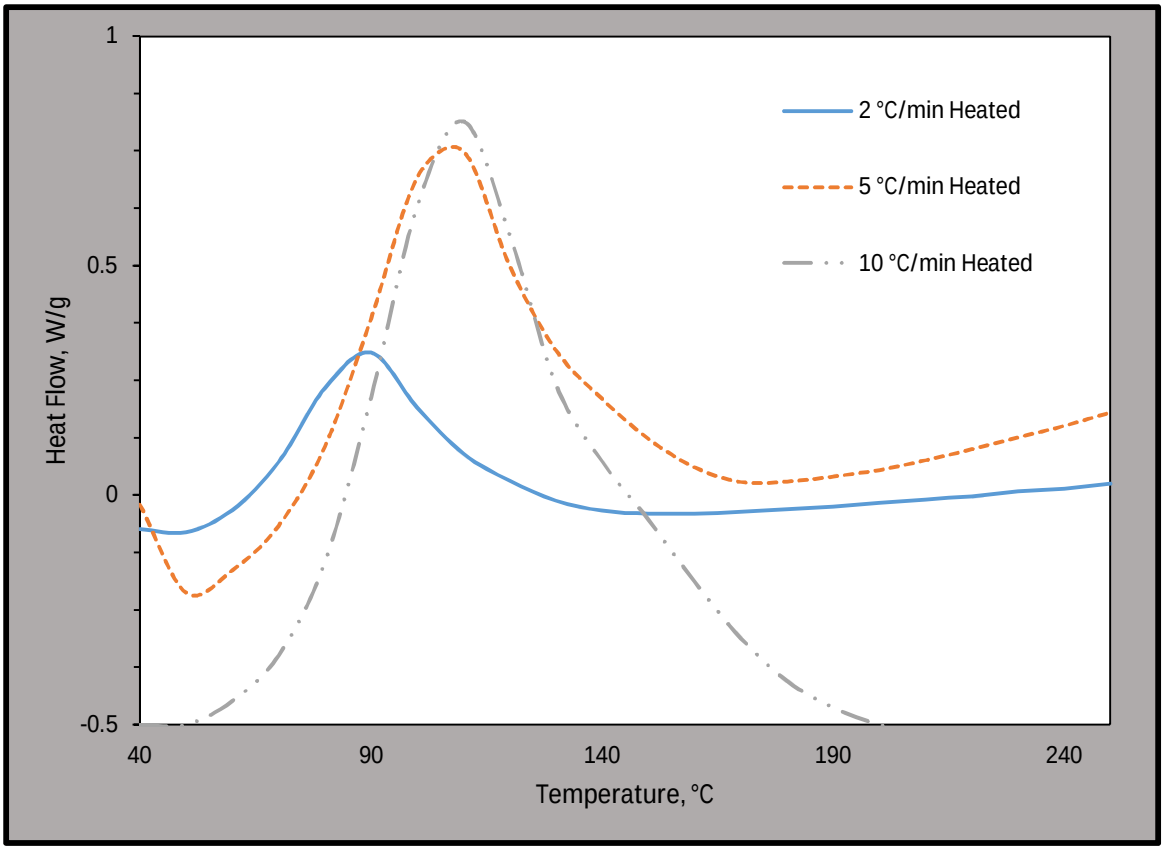

Figure 22: Dynamic DSC with heating epoxy resin at heating rates 2 °C/min, 5 °C/min, and 10 °C/min

Once again each heating rate was done five times for consistency. At a heating rate of 2 °C/min the average peak curing temperature was 87.53 °C with an average onset temperature of 59.62 °C with a standard deviation of 0.57 and 2.53 respectively. Compared to no prior heating of the epoxy resin, the peak curing temperature did not

vary significantly. However, there was a few degrees difference in the average onset temperatures though the significance of the difference is small.

The heating rate of 5 °C/min had an average peak curing temperature of 105.93 °C and an average onset temperature of 73.16 °C with a standard deviation of 1.78 and 1.89 respectively. At the same heating rate, but without prior heating of the resin, the peak temperature was 108 °C. Therefore, there is not much difference in the peak curing temperature between with and without prior heating of the epoxy. The average onset temperatures for both with and without prior heating of the epoxy resin were fairly similar as well within 2.02 °C.

At the heating rate of 10 °C/min, the average peak curing temperature was 121.30 °C with an average onset temperature of 83.07 °C with a standard deviation of 0.98 and 1.36 respectively. Once again, the peak curing temperatures for the same heating rate but with and without prior heating (124.60 °C) was fairly comparable. The onset temperatures varied by a few degrees but the significance is small. Therefore, the isothermal DSC could be done without prior heating of the epoxy resin.

The maximum curing temperatures were determined from the dynamic DSC curves. The onset temperature for the heating rate of 10 °C/min was determined by integrating the peak using the TA Instruments Universal Analysis software seen in Figure 23 below and the values for the peak integration are given in Table 5.

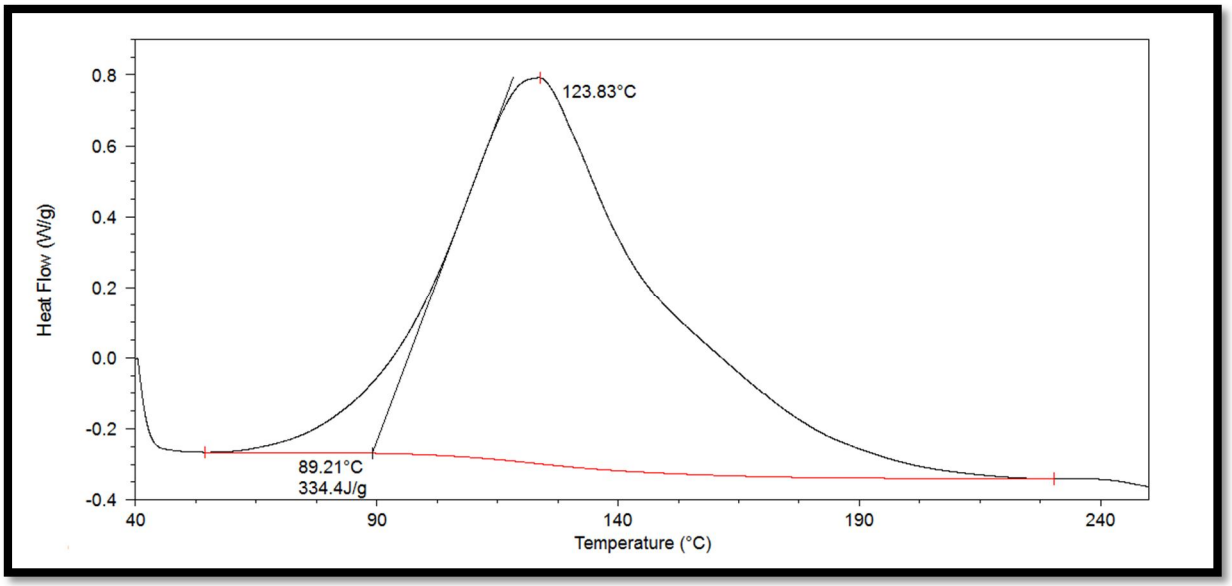

Figure 23: Determination of onset temperature for 10 °C/min from dynamic DSC

Table 5: Values for Dynamic DSC Peak Integration

Peak Integration				
Start T, °C	**Onset, °C**	**Peak T, °C**	**End T, °C**	**ΔH, J/g**
54.4	89.21	123.83	230.30	334.40

The onset temperature for 10 °C/min was approximately 90 °C. Thus, the isothermal DSC measurements of the resin were conducted from 50 °C to 80 °C at intervals of 10 °C for 100 minutes and the results are seen in Figure 24 below.

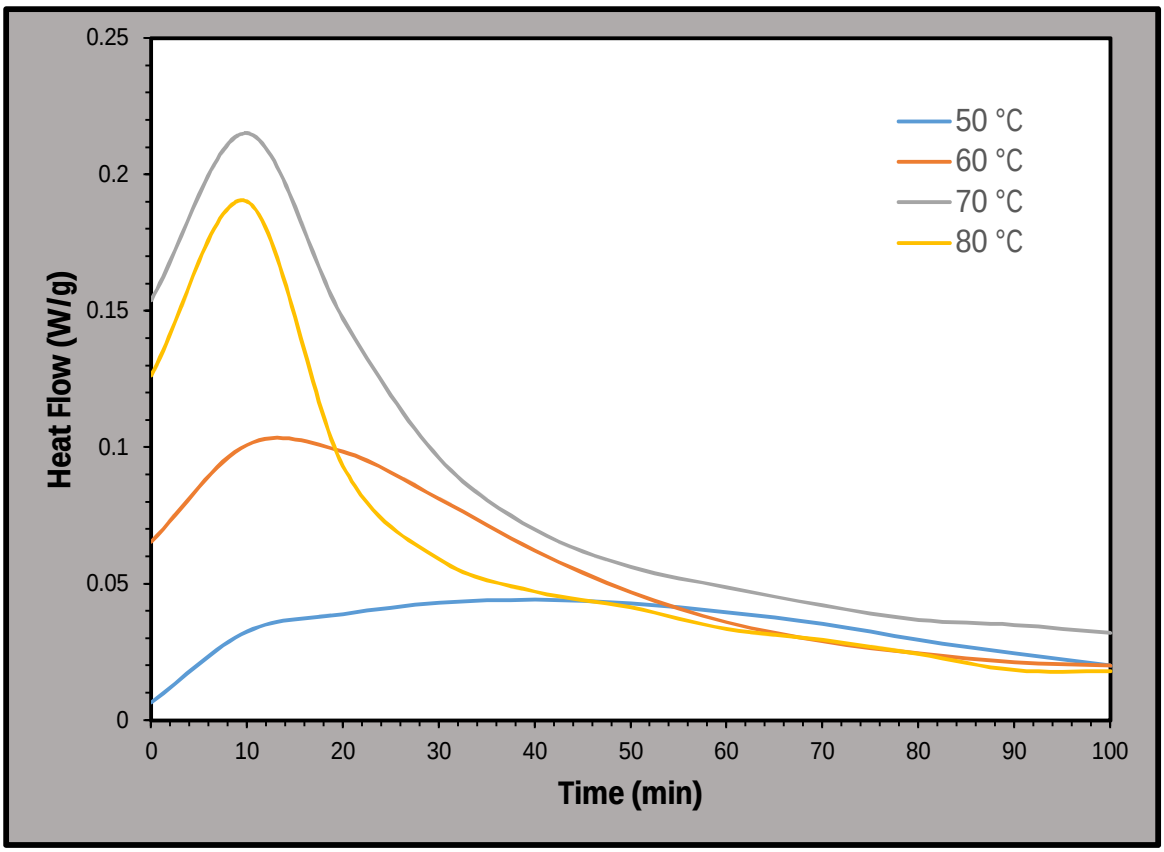

Figure 24: Isothermal DSC curves at 50 °C, 60 °C, 70 °C, and 80 °C

As expected, at higher temperatures the maximum point of the peak appears in a shorter amount of time. At 70 °C and 80 °C, the amount of time was comparatively the same though there was a difference in the cure reaction heat released calculated by the integration of the peaks with the TA Instruments Universal software as seen in Figure 25 below.

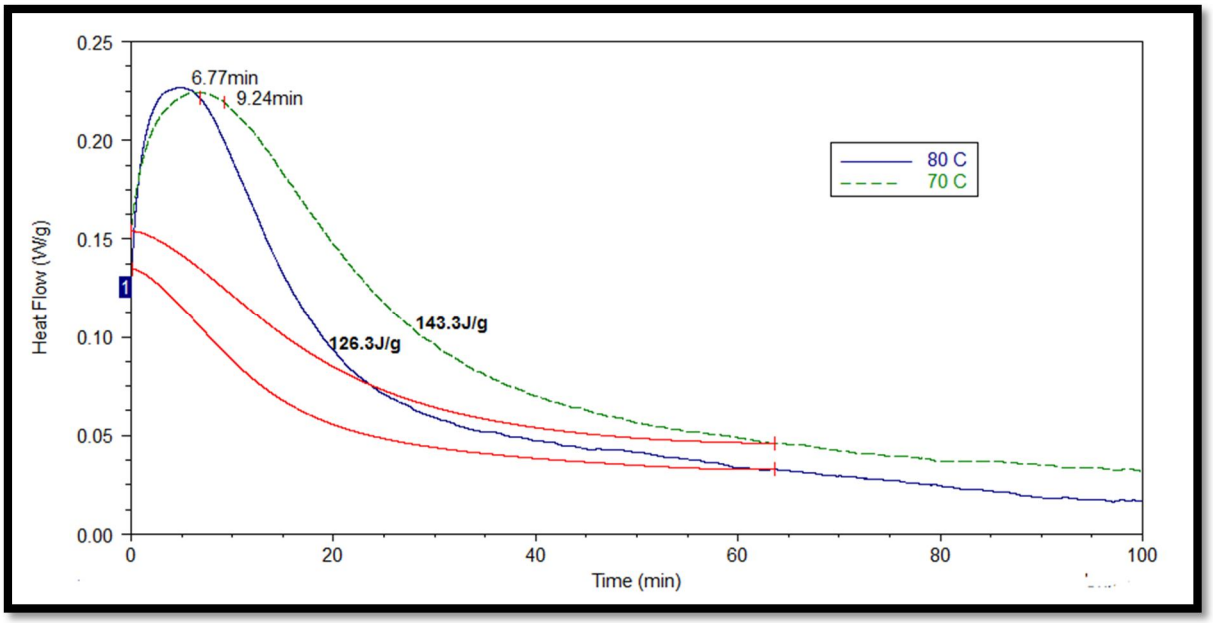

Figure 25: Integration of 70 °C and 80 °C isothermal DSC curves

From Figure 25, the heat released at 70 °C was 143.30 J/g while the heat released at 80 °C was 126.30 J/g. However, at 80 °C, the amount of heat flow from the peak to the end temperature of 63.89 minutes was 0.18 W/g whereas at 70 °C, the heat flow was 0.17 W/g. Because there was not a significant change in the amount of heat flow between the 70 °C and 80 °C but a significant difference in the heat released, 70 °C was used for comparison to the recommended 55 °C.

4.3 Kinetic Modeling

The cure behavior can be further described by relating the DSC analysis to kinetic models. In the kinetic studies by DSC, the heat of reaction, dH(t), is proportional to the degree of cure, α and is defined as:

$$\alpha = \frac{H(t)}{H_U} \qquad (2)$$

where H(t) is the heat of reaction up to time, (t) calculated from the area under the isothermal DSC curve and H_U is the total heat of reaction measured in the dynamic DSC tests. The rate of reaction, $\frac{d\alpha}{dt}$, can be defined as:

$$\frac{d\alpha}{dt} = \frac{1}{H_U}\frac{dH(t)}{dt} \tag{3}$$

The rate of reaction is dependent on the temperature, and the Arrhenius equation can be defined as:

$$k = A \exp\left(-\frac{Ea}{RT}\right) \tag{4}$$

where k is the temperature dependent rate constant, E_a is the activation energy, A is the pre-exponential factor, R is the universal gas constant, and T is the absolute temperature. The rate of reaction of the epoxy curing reaction can then be defined as the following expression:

$$\frac{d\alpha}{dt} = A \exp\left(-\frac{Ea}{RT}\right) f(\alpha) \tag{5}$$

where $f(\alpha)$ is the reaction model. There are several kinetic models that can describe the cure behavior of thermosets. Typically reaction models for thermosets are described by n^{th} order or autocatalytic models where $f(\alpha) = (1-\alpha)^n$ or $(1-\alpha)^n(1+k_{cat}\alpha)$ respectively.

One method used to determine the kinetic parameters is the Kissinger method. The Kissinger method assumes that the activation energy and pre-exponential factor are constant throughout the dynamic DSC and assumes a first order reaction. This means that for each heating rate, the Kissinger method looks at one data point, the peak temperature. The Kissinger method can be defined as:

$$\ln\left(\frac{\beta}{T_p^2}\right) = \ln\left(\frac{AR}{E_a}\right) - \frac{Ea}{RT_p} \quad (6)$$

where T_p is the peak temperature. The E_a and A can be estimated by plotting $\ln\left(\frac{\beta}{T_p^2}\right)$ versus $\frac{1}{T_p}$ as seen in Figure 26 below.

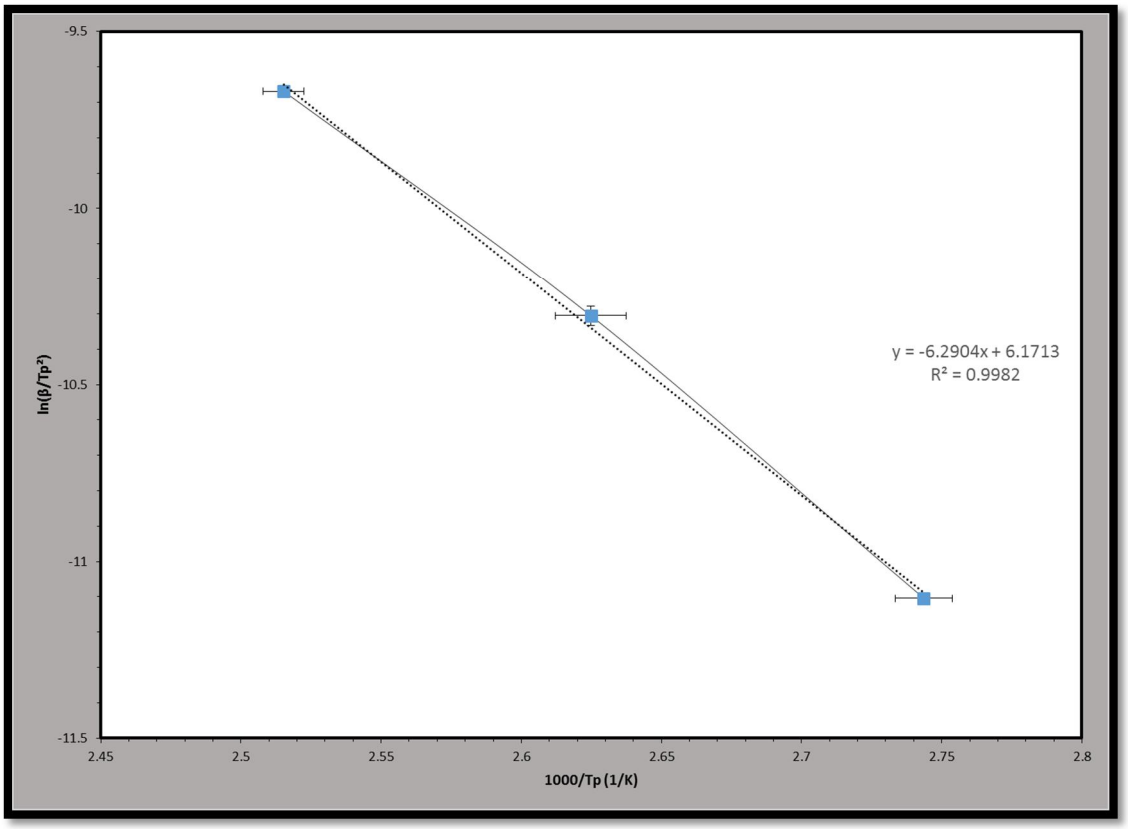

Figure 26: Plot of $\ln\left(\frac{\beta}{T_p^2}\right)$ versus $\frac{1}{T_p}$ showing linear kinetic relationship

The E_a and A can be calculated from the linear fit of the slope and intercept. To calculate E_a, the slope is multiplied by the universal gas constant, and estimated to be approximately 52.30 kJ/mol. To calculate A, the intercept of 6.1713 is set equal to $\ln\left(\frac{AR}{E_a}\right)$ giving an estimate of approximately 3.01 x 10^3 min^{-1}.

Another method to calculate E_a is the Ozawa-Flynn-Wall method. The difference between this method and the Kissinger is that Ozawa assumes that E_a is a function of the degree of cure. As a function of the degree of cure, E_a is not constant throughout the reaction. Ozawa method can be expressed by the following equation:

$$E_a = -\frac{R\,\Delta \ln(\beta)}{1.052\,\Delta\left(\frac{1}{T_p}\right)} \tag{7}$$

Thus the E_a can be determined by plotting ln (β) versus $\left(\frac{1}{T_p}\right)$ as seen in Figure 27 below.

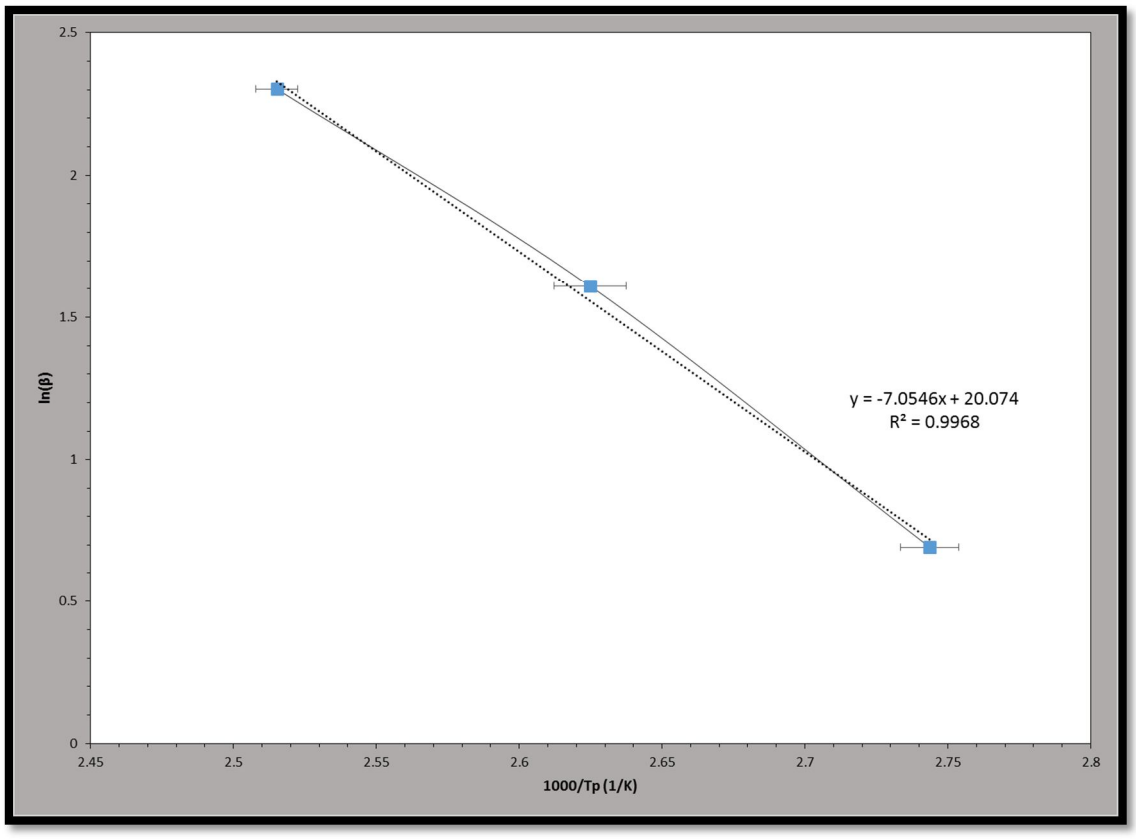

Figure 27: Plot of ln (β) vs. $\frac{1}{T_p}$showing the kinetic linear relationship

Once again, the E_a can be calculated by the linear fit of the slope and intercept. For E_a the slope is multiplied by the gas constant and divided by 1.052 and is estimated to be approximately 55.75 kJ/mol.

From Kissinger, the E_a was estimated to be around 52.30 kJ/mol while from Ozawa, the E_a was estimated to be approximately 55.75 kJ/mol. Ozawa has a slightly higher estimate than Kissinger, but the values are fairly similar and either can be used to approximate the activation energy. The activation energy is the minimum energy required to start a chemical reaction. As the heating rate increases, the faster the rate of reaction which expedites the degree of cure where $\alpha = 0$ (completely uncured) to $\alpha = 1$ (completely cured).

4.4 Characterization

How well the epoxy can infiltrate and protect the pores in TBCs with or without heating prior to mounting at ramp rates of 2 °C/min, 5 °C/min, and 10 °C/min to 55 °C or 70 °C can be characterized by optical microscopy. A standard procedure from industry was closely followed for the grinding and polishing process. The ultimate goal was to determine if the curing rate and temperature at which the samples were mounted would protect the pores present in the coating to possibly eliminate variability in the sample preparation in order to accurately characterize TBCs. Measurements on the percent porosity was done to characterize the performance of the epoxy.

4.4.1 Percent Porosity Measurements

Optical images were taken using the Olympus BX51 and percent porosity measurements were done using the complimentary Olympus Stream software. The images were taken in brightfield under 100x magnification with a 10x objective lens. A region of interest (ROI)

defined the area to be measured and the minima and maxima threshold separates the epoxy filled pores from the YSZ coat, bond coat, and substrate. The threshold was held constant for all measurements at a maxima of 103. For each sample, five measurements for porosity percentage were calculated and averaged.

At a heating rate of 2 °C/min to 55 °C samples 1, 2, and 3 had consistent porosity measurements with an average of 29.33%, 33.08%, and 27.55% respectively. The high percentages can be explained by the large cracking across the coating. A microstructure of the crack in the coating is shown in Figure 28 below.

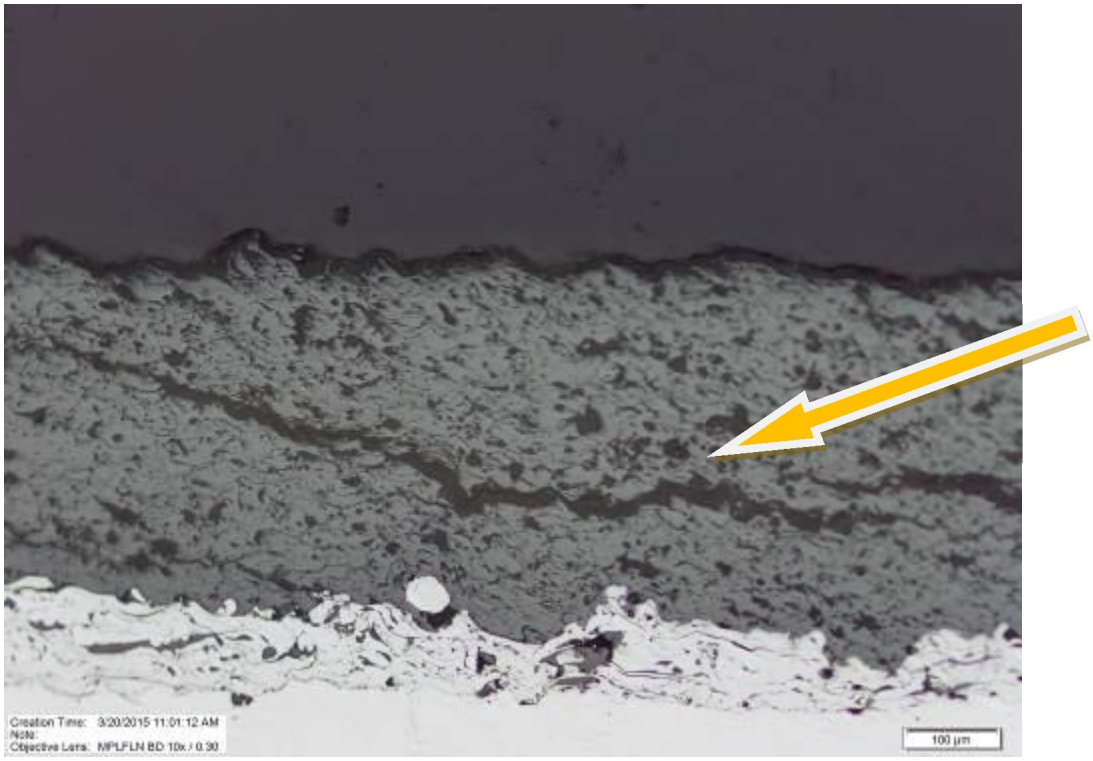

Figure 28: Microstructure of 2 °C/min to 55 °C with crack in coating but with full epoxy infiltration

Figure 28 above shows a variety of characteristics in the TBC layer. There are voids, crack-like inter-splat voids, particles that did not melt, and a noticeable large cracking across the coating. The large crack in the coating could have been caused by the original spray process or sectioning damages. Although the large crack is present, the epoxy, seen in a light shade of grey, had completely infiltrated the crack as seen in a 3D imaging from ImageJ in Figure 29 below.

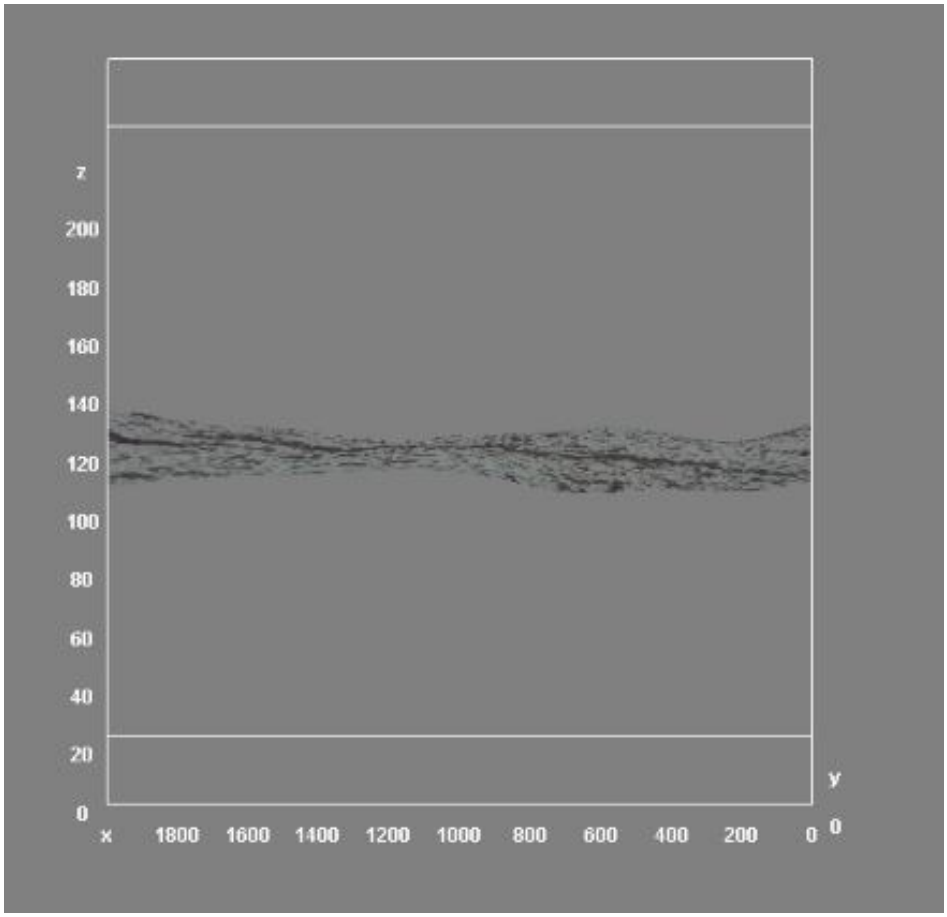

Figure 29: 3D imaging of Figure 28 by ImageJ

From Figure 29 above, though there may seem like there are no pullouts present, the surface is not completely smooth. This could be due to the grinding and polishing process

where there was not a sufficient amount of time to planarize the surface. Another image of a crack was taken and shown in Figure 30 below.

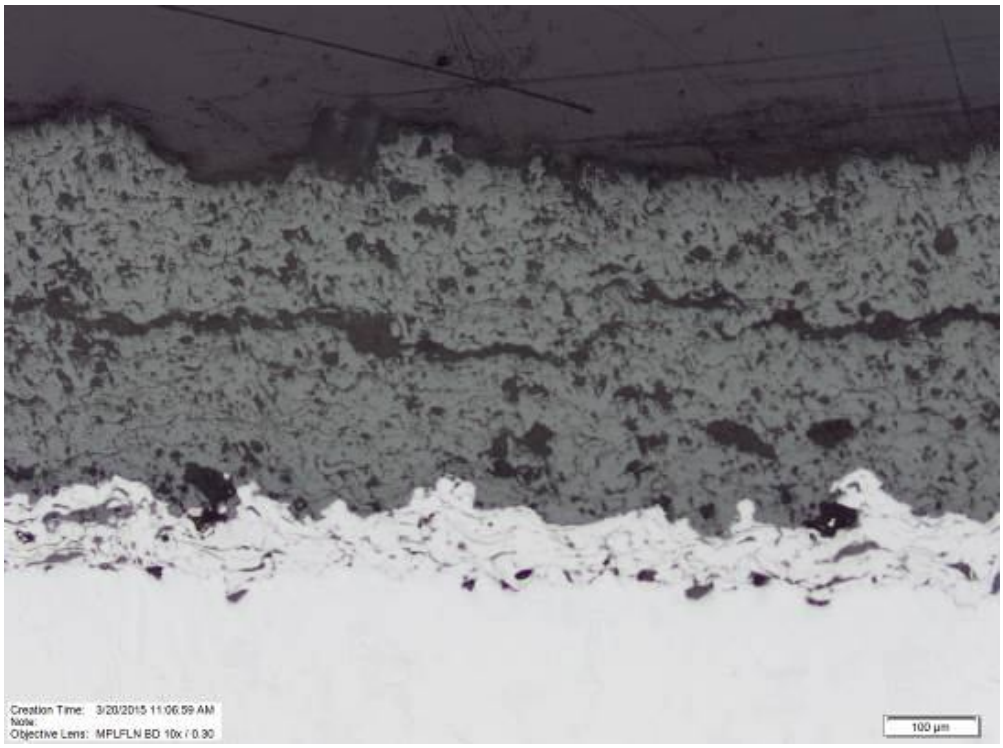

Figure 30: Microstructure of 2 °C/min to 55 °C with epoxy infiltration in cracks and pores

In Figure 30 above, the cracks are filled with the epoxy almost entirely. There are little to no pullouts within the coating and the filling of the pores can be seen in Figure 31 below.

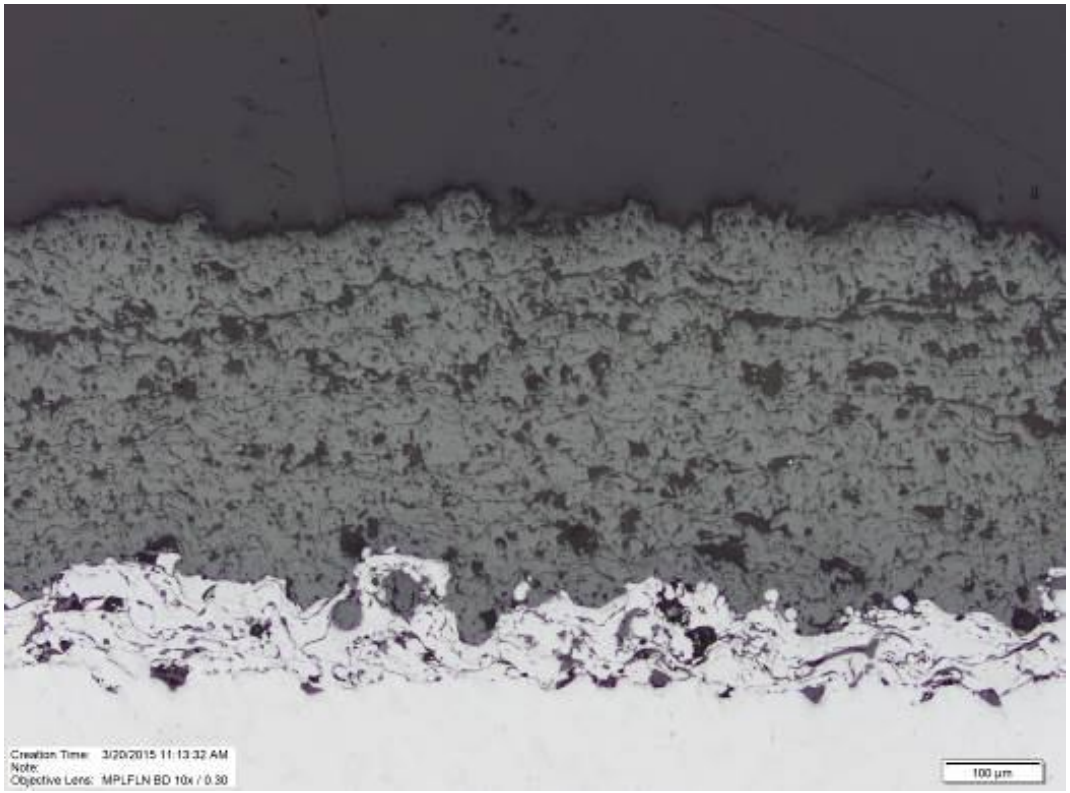

Figure 31: Microstructure of 2 °C/min to 55 °C with complete impregnation in pores

Figure 31 above shows that the epoxy was able to impregnate the pores and remain intact during grinding and polishing. At 5 °C/min to 55 °C, the cracking issue is present once again but at this curing rate, the crack is not fully impregnated seen in Figure 32 below.

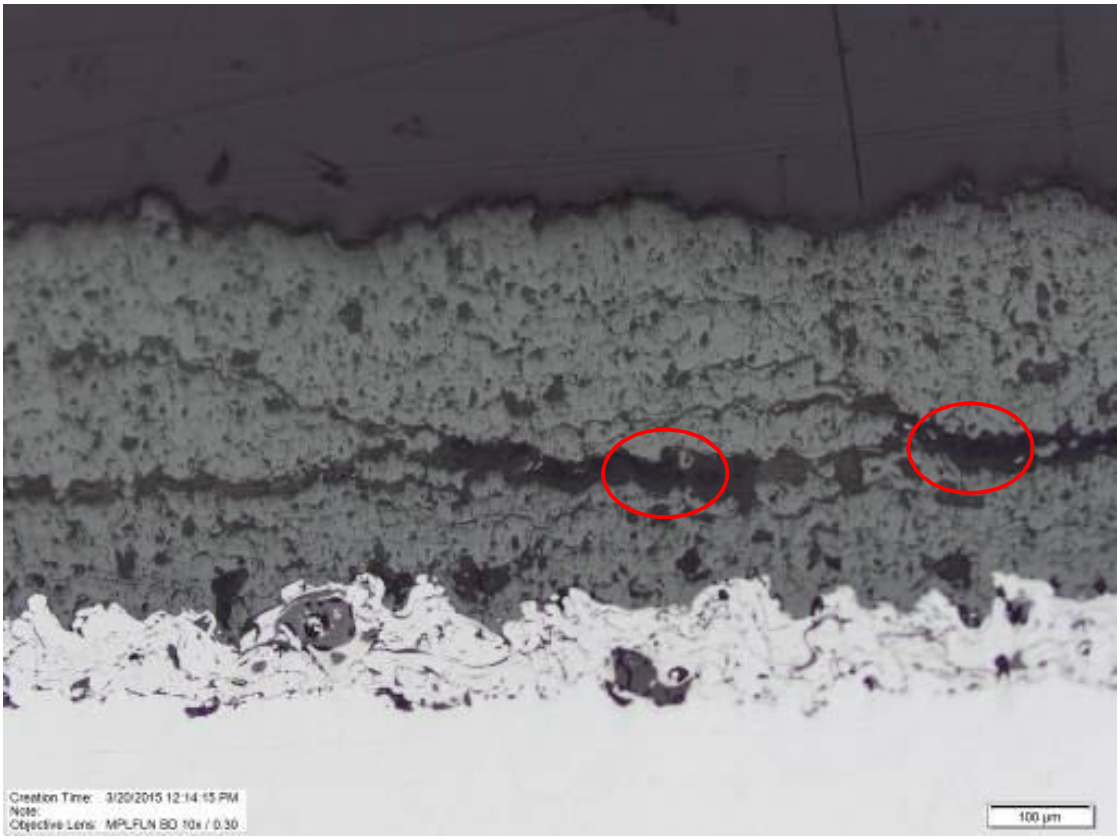

Figure 32: Microstructure at 5 °C/min to 55 °C with crack without complete infiltration of the epoxy

As seen in Figure 32 above, there is a large crack across the coating. The epoxy was either pulled out during grinding or never fully filled during the cure. A close up of the same crack with 20x magnification can be seen in Figure 33 below.

Figure 33: Microstructure of 5 °C/min to 55 °C under 20x magnification of crack

From the above figure, the crack is seen under higher magnification to show the incomplete penetration of the epoxy. However, it is difficult to say what the image is showing without 3D imaging or SEM. The average percent porosity measurements were high with an average of 38.36%. This measurement accounts for the cracks and pull outs in coating thus masking the true porosity.

At a heating rate of 10 °C/min to 55 °C, the average percent porosity was approximately 27.06%. A microstructure of a sample region is seen in Figure 34 below.

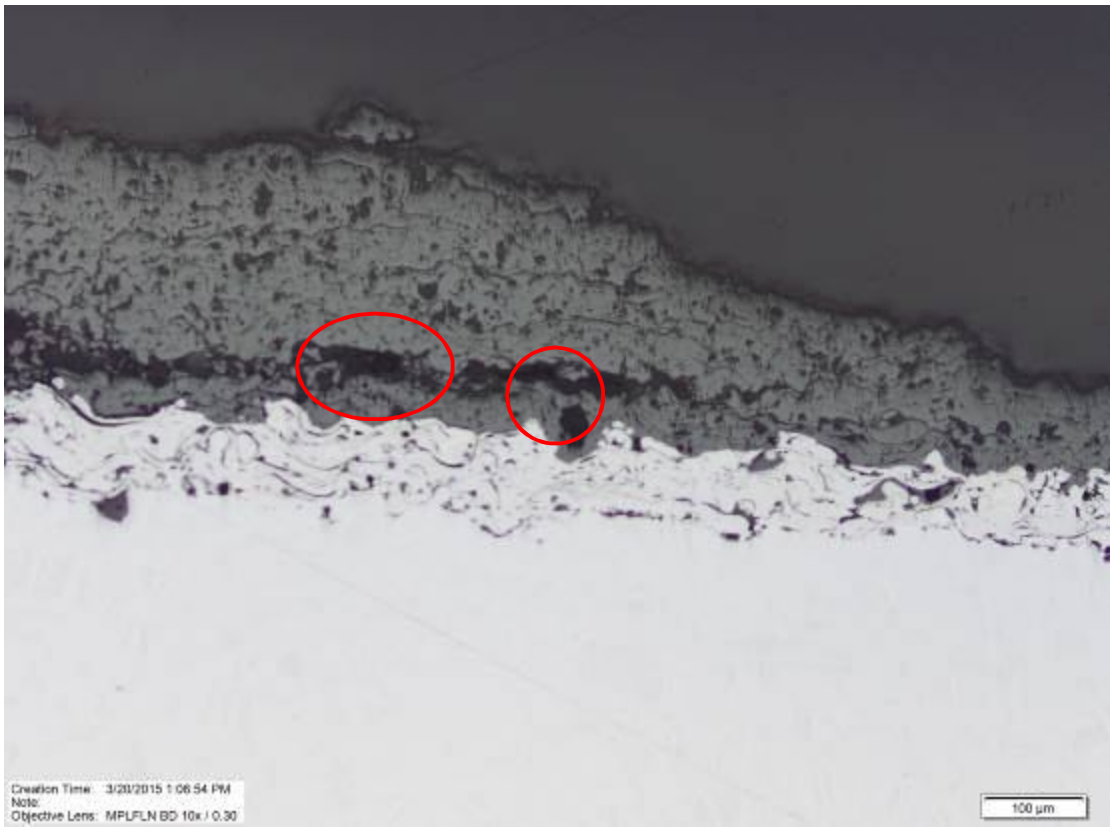

Figure 34: Microstructure of 10 °C/min to 55 °C

In Figure 34 above, the coating is uneven compared to the previous images. This is due to the chipping and damaging of the coating during sectioning. The purpose of the grinding procedure is to eliminate the damages caused by sectioning, however from this procedure, the allotted time did not seem to be enough to remove those damages. In this same image, cracking is prominent once again with a lack of epoxy filling. Another image in Figure 35 below shows the lack of time during grinding.

Figure 35: Microstructure of 10 °C/min to 55 °C with uneven surface

In Figure 35 above, the microstructure is out of focus as highlighted by the rectangles. This means that the cross section was not completely planar before moving to the next steps of the grinding and polishing stages. The coating is once again uneven and shows that the damages caused by sectioning were not removed.

When the samples were placed into the furnace at 55 °C without a controlled ramp rate, the average percent porosity was approximately 26.18%. Once again, the issue of a dense coating image was likely due to the amount of time spent on grinding. A microstructure of the coating can be seen in Figure 36 below.

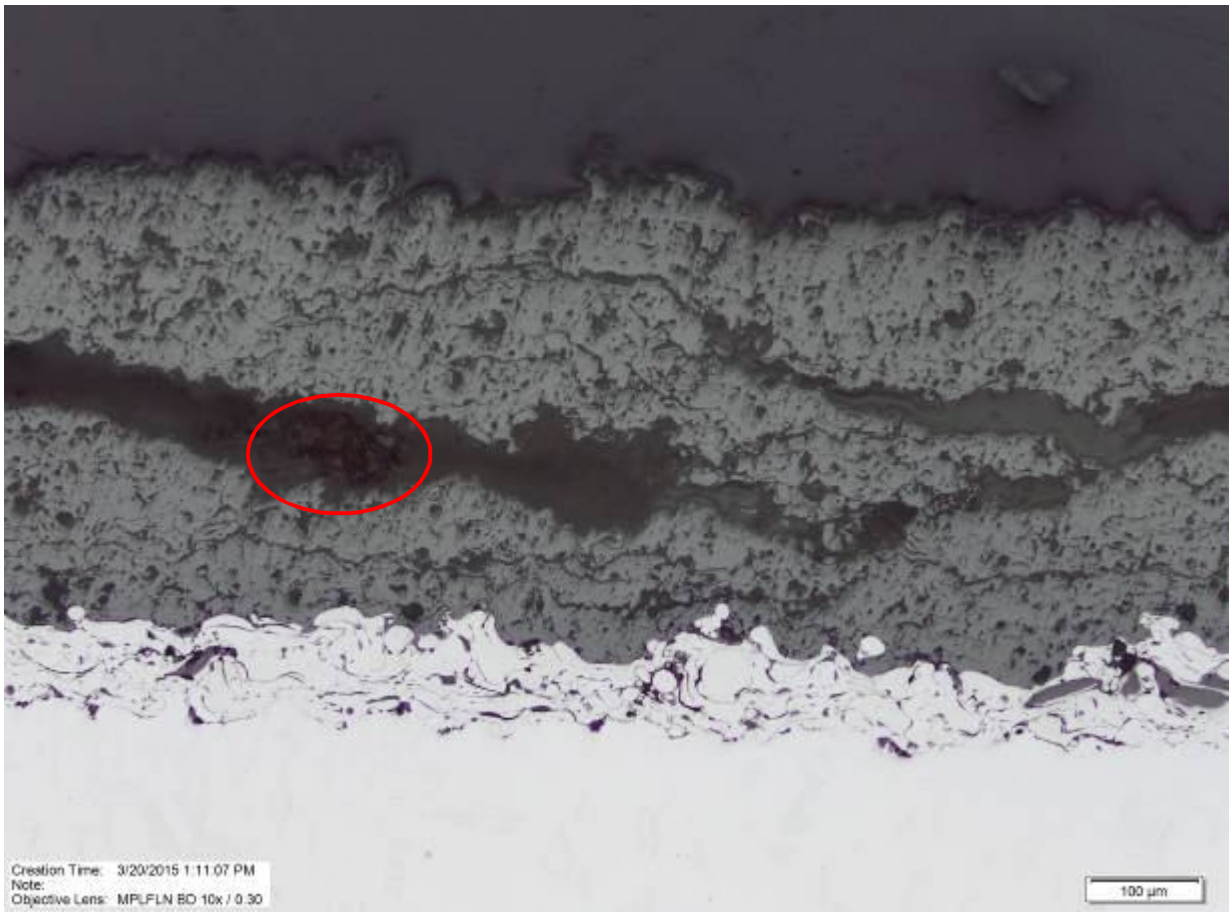

Figure 36: Microstructure at no rate of 55 °C

The above figure shows ambiguity whether or not epoxy was ground off or if the crack was indeed that size. The highlighted circle shows that there could be pullout where the epoxy was unable to protect the coating. Another problem that can be seen is smearing which occurs when the metal from the bond coat fills the pores and obscures the focus of the coating. Another microstructure is shown in Figure 37 below.

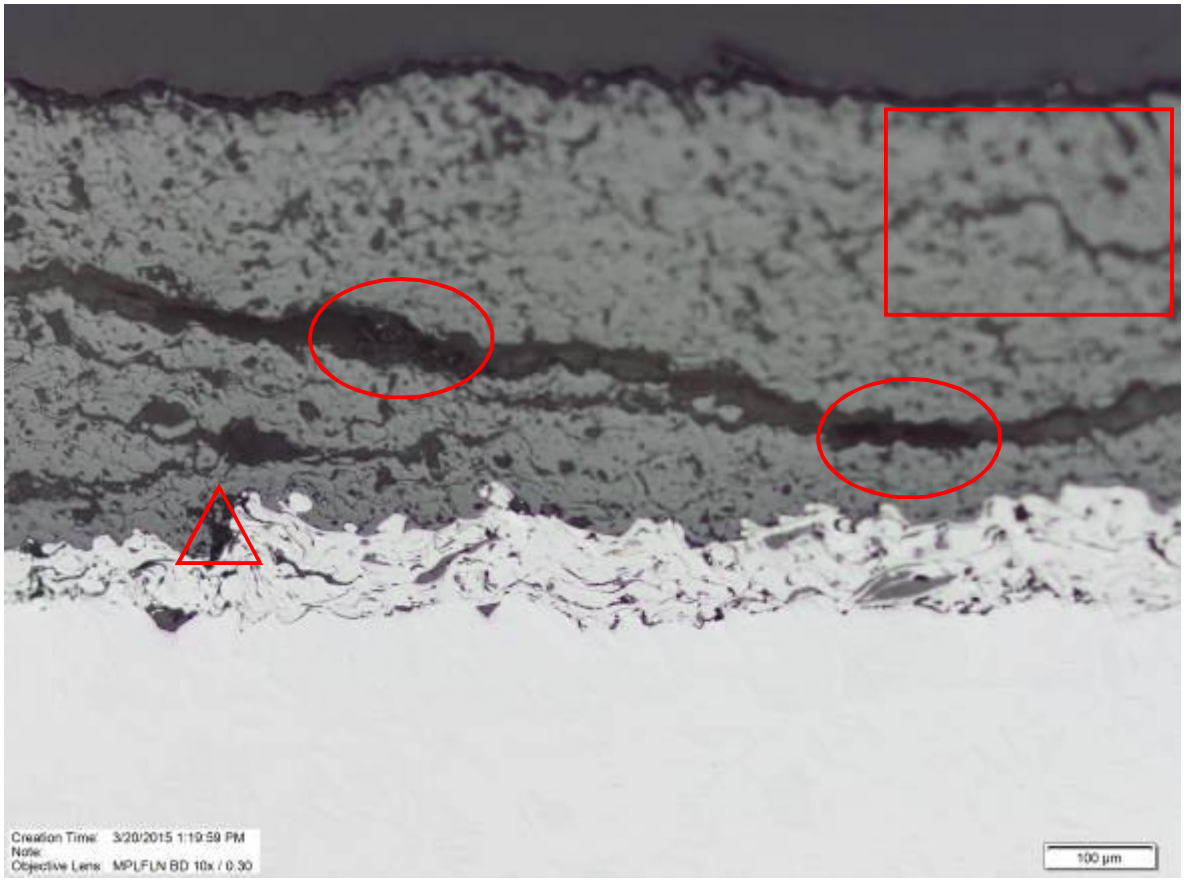

Figure 37: Microstructure at no rate of 55 °C

In Figure 37, the rectangle highlight shows that the sample surface is out of focus meaning that the surface is not completely flat. The circles show imperfections within the coating. However, the imperfections are difficult to determine and could be the mixing of two phases, pull out, or TGO present in the coating. The triangle highlight shows that there is some delamination of the TBC from the bond coat. This could be due to the epoxy not being able to penetrate completely through the coating.

When the resin was heated prior to mounting the sample at 2 °C/min to 55 °C, the average percent porosity was approximately 25.44%. However, this average was done from one of the three samples. The other two samples were not ground and thus the

sectioning damage had not been ground away. Even though one of the samples seemed to be ground, there was not a complete infiltration of the pores as seen in Figure 38 below.

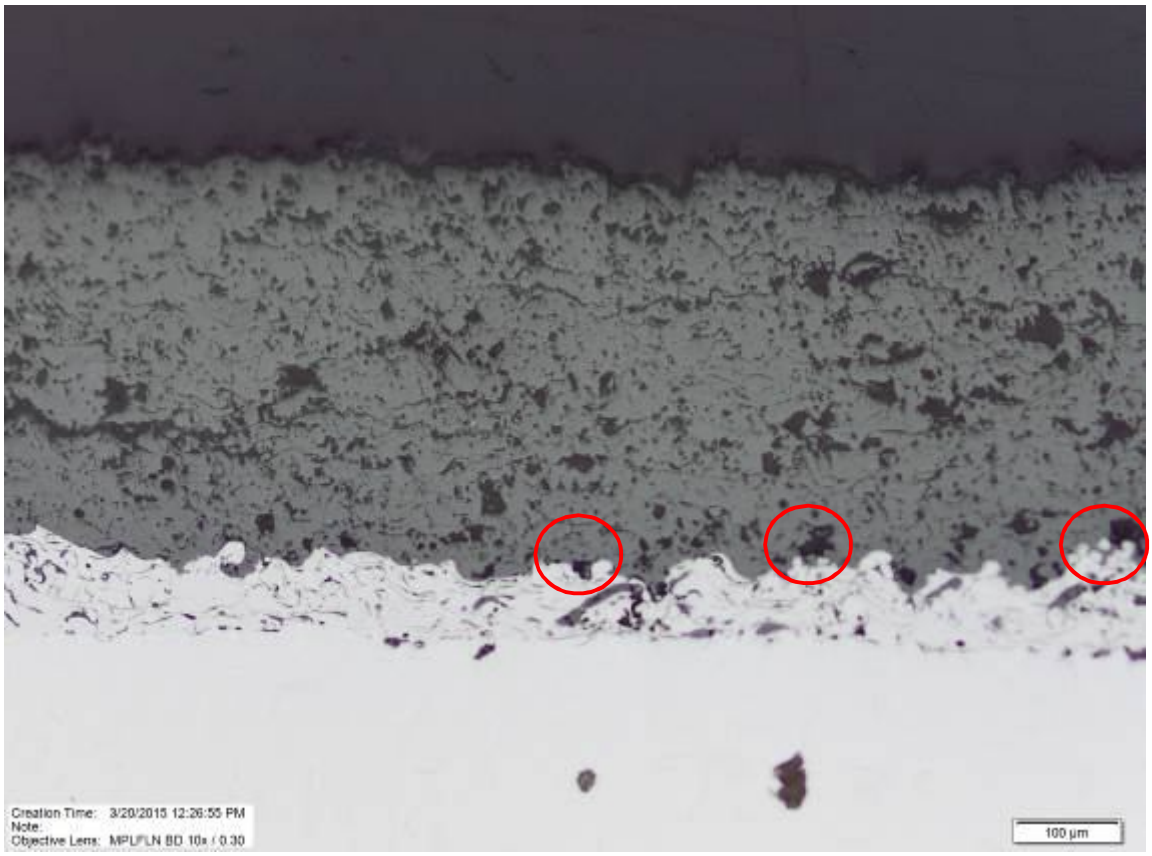

Figure 38: Microstructure at 2 °C/min to 55 °C with prior heating of resin before mounting

Though the epoxy seemed to have penetrated well throughout the coating and maintained the integrity of the surface, there were a few voids near the bond coat. This could have been due to the incomplete infiltration of the epoxy, shrinkage, or due to pull out from grinding and polishing. Another microstructure at this same parameter can be seen in Figure 39 below.

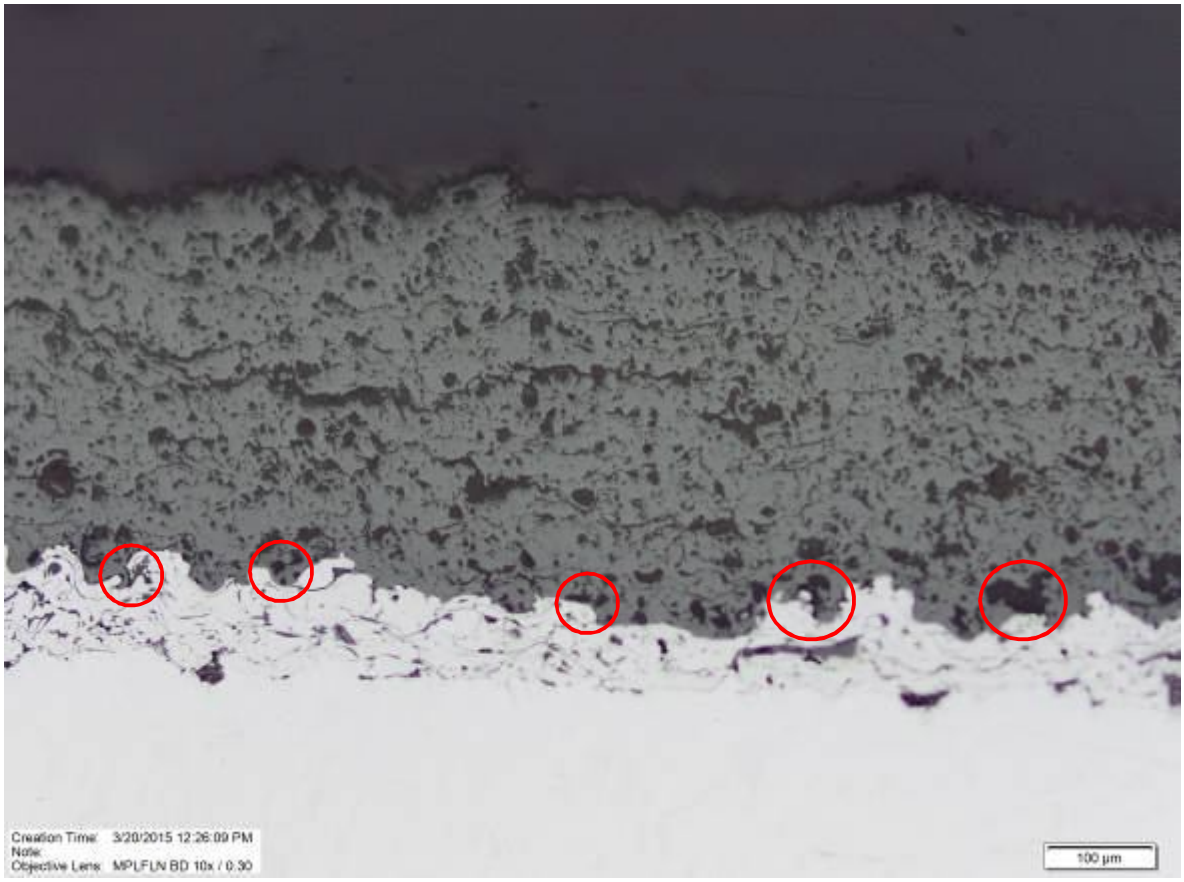

Figure 39: Microstructure at 2 °C/min to 55 °C with prior heating of resin before mounting of another sample

From Figure 39, the pores once again seem to be infiltrated well by the epoxy. The TBC layer seems to be delaminating from the bond coat which will lead to coating failures. The epoxy was able to protect the coating with minimal shrinkage.

When the epoxy was heated prior to mounting at a rate of 5 °C/min to 55 °C, the samples were once again not planar or ground. The percent porosity was not measured, but an image of the microstructure can be seen in Figure 40 below.

Figure 40: Microstructure of epoxy heated prior to mounting at 5 °C/min to 55 °C

From Figure 40, the image is out of focus because the surface is not planar is due to the lack of time during grinding. However it can also be noted that the epoxy was unable to penetrate and retain protection within the cracks as seen by the highlighted circles. The curing may have been done much quicker and thus caused shrinkage or brittleness of the epoxy. Images were taken with the ESEM under low vacuum pressure and at a tilt of 51° seen in Figure 41 below.

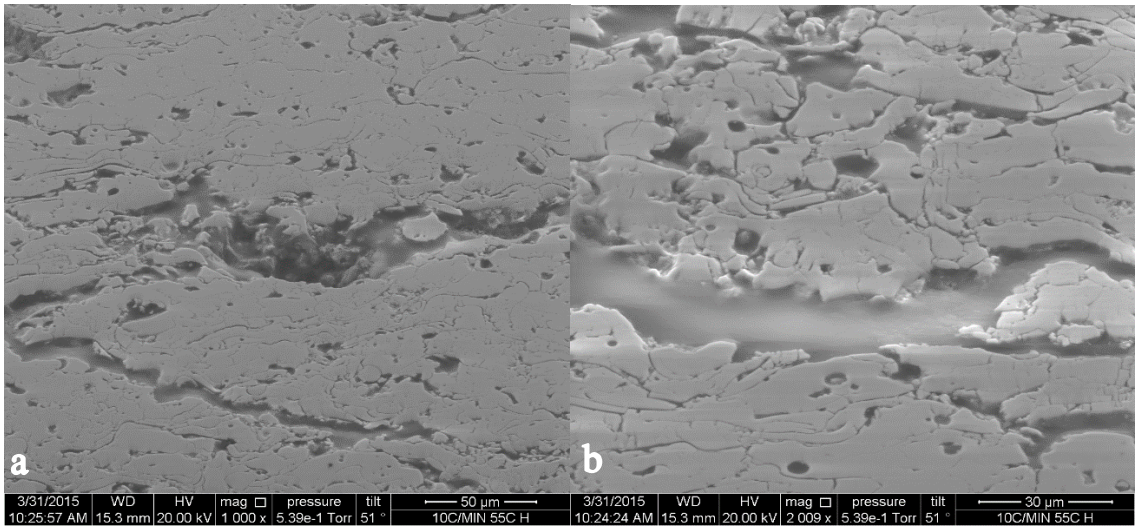

Figure 41: Microstructure taken with ESEM under low vacuum at 1000x magnification and 2009x magnification repectively and tilted at 51°

By using the ESEM, the microstructure of the coating could be characterized more clearly. The large crater in Figure 41a shows that the epoxy was unable to protect the coating thus resulting in a pullout. Figure 41b shows that the epoxy was able to maintain within the crack however the edge of the crack seems to be higher than the epoxy. The differences in level was probably due to the epoxy being ground off quicker than the coating.

A few samples were damaged or the grinding time was not long enough to remove sectioning damages. As a consequence, the threshold in the analysis software was unable to distinguish between the pores and coating. The porosity measurements are listed in Appendix B. At a heating rate of 2 °C/min to 70 °C with prior heating of the epoxy resin, the microstructure can be seen n Figure 42 below.

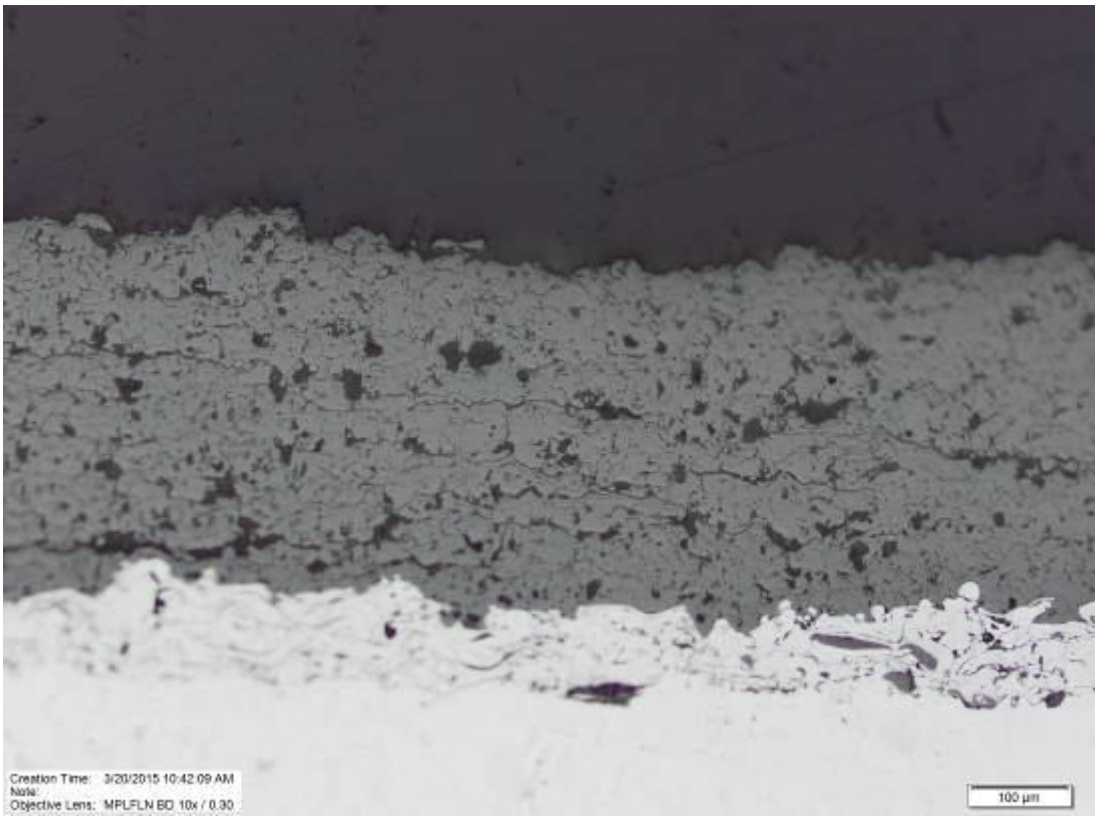

Figure 42: Microstructure at heating rate of 2 °C/min to 70 °C with prior heating of the epoxy resin

In the above figure, the sample was ground enough to characterize the percent porosity. The average porosity percent was approximately 17.42%. From the image, the pores seem to be impregnated and well protected by the epoxy. The curing reaction was much slower which means a more controlled curing and penetration by the epoxy. As the temperature rate increased to 5 °C/min with and without prior heating of the epoxy resin, poor impregnation was observed as seen in Figures 43 and 44 below.

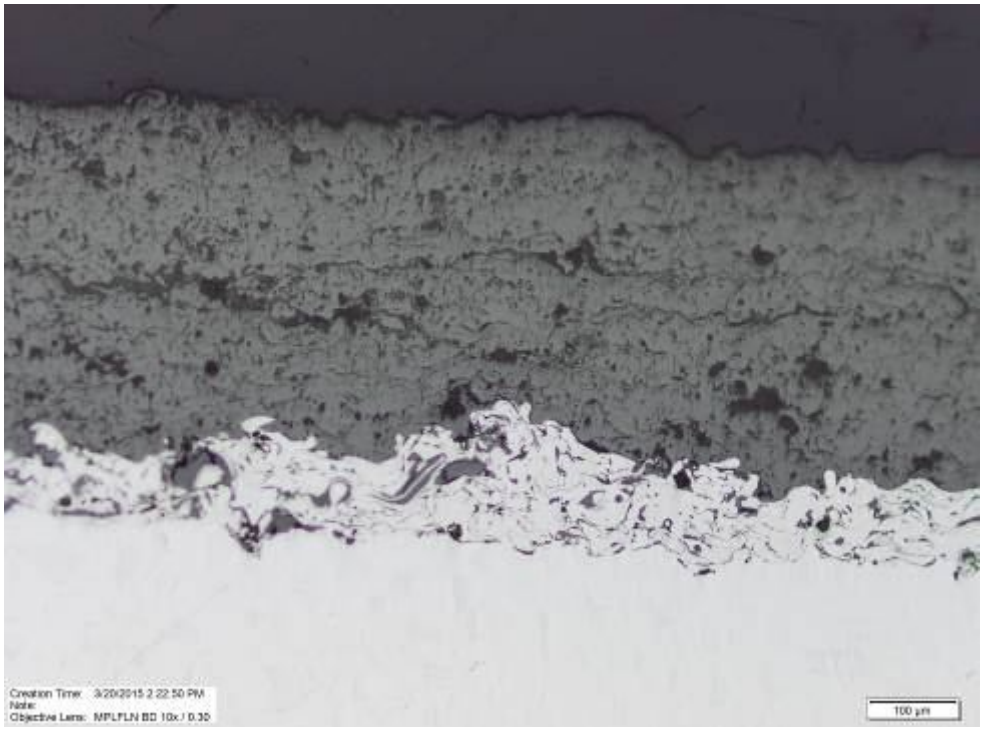

Figure 43: Insufficient epoxy infiltration at 5 °C/min to 70 °C without prior heating of epoxy resin

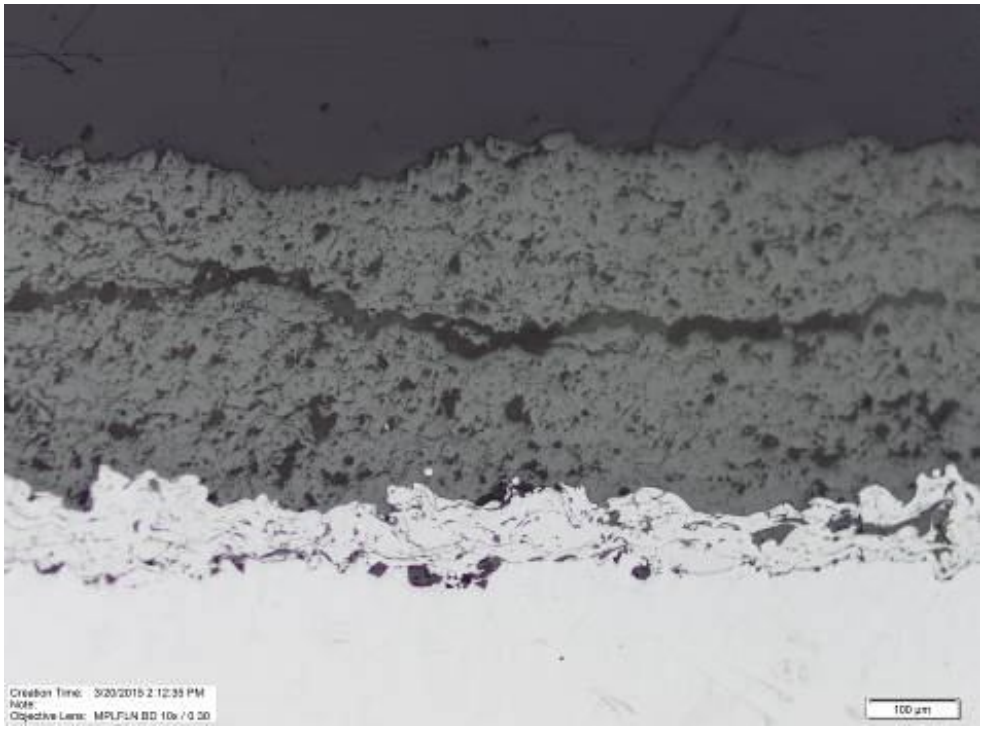

Figure 44: Coating damage and insufficient filling from epoxy at 5 °C/min to 70 °C with prior heating of epoxy resin

The increase in heating rate to 5 °C/min to 70 °C seemed to have an effect on how well the epoxy maintained its integrity within the pores with or without prior heating of the epoxy. As seen in Figures 43 and 44 above, like the other samples there is noticeable cracking, however in this situation the epoxy was unable to reside within the pores and crack.

With further heating at a rate of 10 °C/min to 70 °C with prior heating of the epoxy resin, poor infiltration of the epoxy can be seen in Figure 45 below.

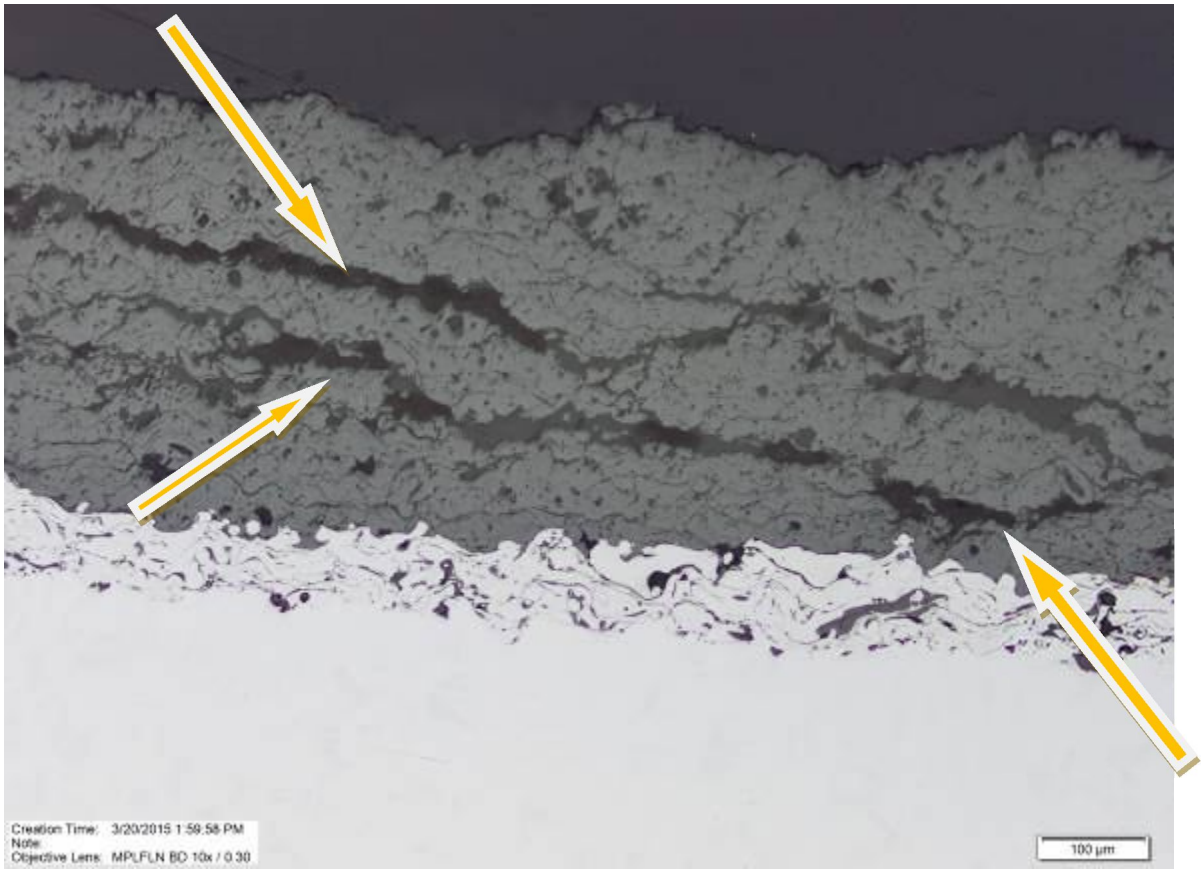

Figure 45: Microstructure at heating rate of 10 °C/min to 70 °C with prior heating of the epoxy resin

In Figure 45 above, there is a significant amount of cracking is present in the sample. This could be from the sectioning process that was not ground away or that the spraying itself was at fault. However, the main focus is how well the epoxy penetrated and protected even the cracking. In this case, the epoxy did not seem to be able to penetrate and protect the coating from further damage as seen in the discoloring throughout the cracks. The curing rate may have been too high in this instance thus effecting the final cure properties of the epoxy.

When the epoxy was not heated and placed into the furnace at the set temperature of 70 °C, the epoxy was unable to impregnate the pores and cracks well enough to prevent damaging during the grinding process as seen in Figure 46 below.

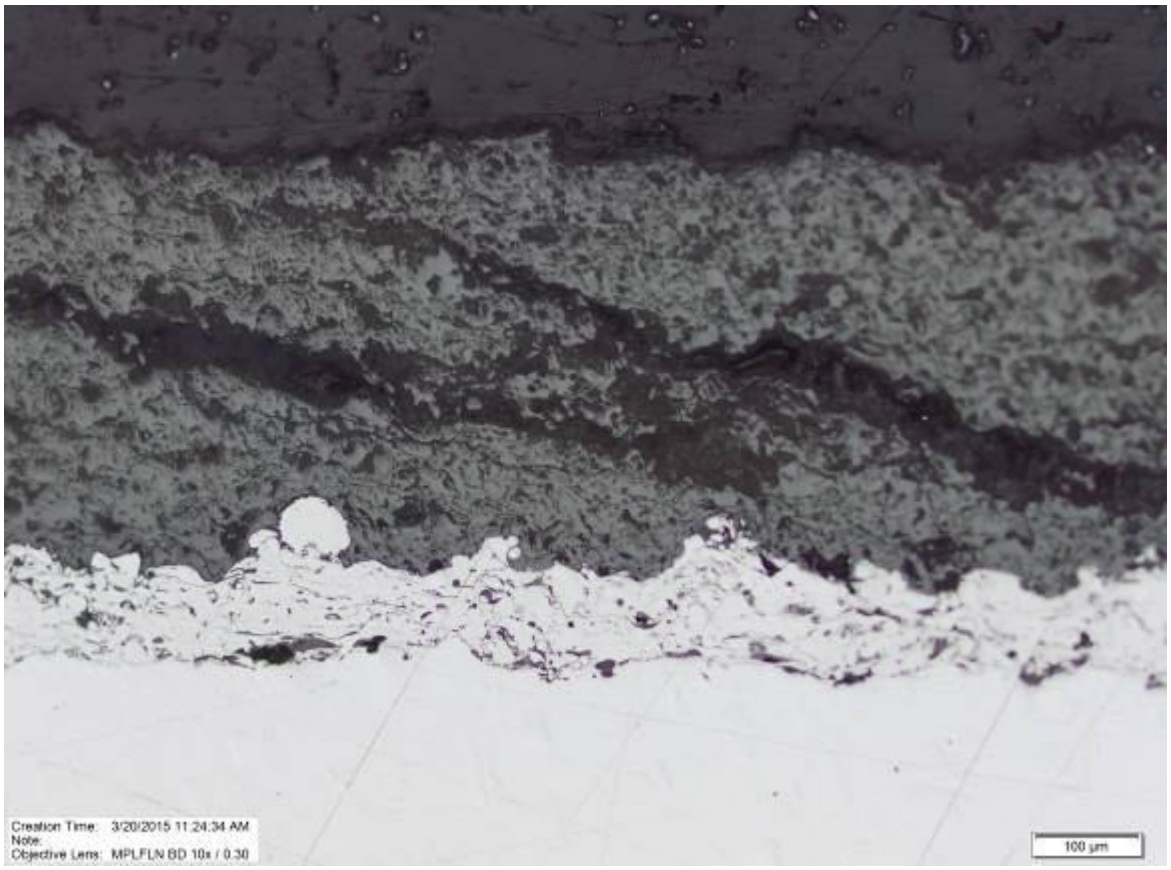

Figure 46: Microstructure at the set temperature of 70 °C

Figure 46 above shows that the sample not being ground and damages caused by the sectioning and grinding stages. The epoxy may have been able to fill the pores but was unable to maintain the adhesion to the coating which could be the reason for the damages seen in the microstructure. Figure 47 below shows a close up of the cracking.

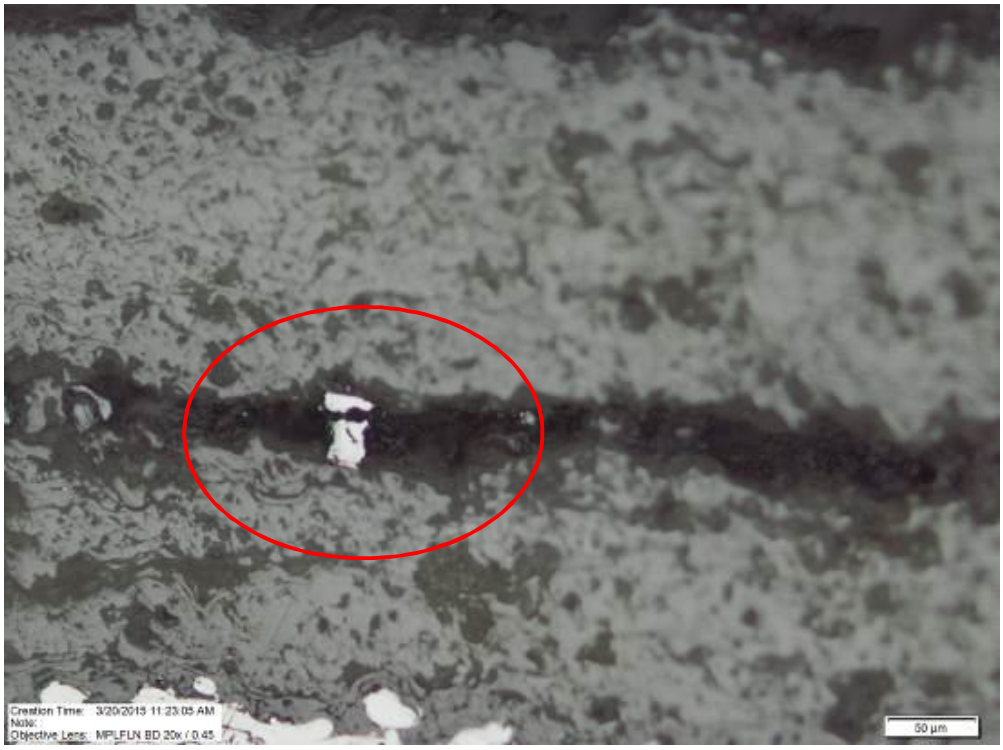

Figure 47: Microstructure of pullout in crack along the coating at 20x magnification

In the above figure, the crack shows the lack of infiltration. The epoxy was unable to protect the coating from further damage thus the pullout can be seen. The uncontrolled curing reaction may have been the reason for this result.

5. Conclusions

The variability in sample preparation of TBCs affect the repeatability in overall characterization of the percent porosity. Inconsistency in these measurements is a concern for coating failures during flight that could lead to catastrophic events. Therefore accurate characterization begins with precise sectioning and mounting of the sample.

This work has studied the curing kinetics of a two part epoxy and the effect on the characterization of TBCs. The samples were sectioned with a low speed precision saw, rinsed with water, soaked in isopropanol alcohol, and dried in ambient temperature. A low viscosity two part epoxy was studied by TGA and DSC. From the dynamic and isothermal DSC thermographs, 70 °C gave the most enthalpy change and thus was the temperature for comparison to the recommended 55 °C for curing. The samples were impregnated with and without prior heating of the epoxy resin and cured at heating rates of 2 °C/min, 5 °C/min, and 10 °C/min to 55 °C or 70 °C. For comparison, samples were also placed in the furnace at a set temperature of 55 °C or 70 °C. The samples were then ground and polished to simulate industry practices.

Finally, the samples were characterized with an optical microscope. The results showed that most samples had major cracking throughout the coating. This could be due to the spraying process or during sectioning. Many samples were not planar after grinding or the damages caused by sectioning had not been removed. The grinding process would need to be studied more in depth, however, the goal of this research was to be able to see

whether the curing kinetics of the epoxy had an effect in protecting the porous coating from further damage during the grinding and polishing stages.

From this study, the best impregnation of the coating and edge retention was from a slow heating rate of 2 °C/min to 55 °C. At the same heating rate of 2 °C/min to 70 °C, the edge retention and integrity of the coating was maintained. However, once the heating rates increased to 10 °C/min or at an uncontrolled heating rate, the impregnation properties of the epoxy resin failed to protect the coating. The amount of pullout increased due to shrinkage from the pores edge. This can be explained by the rate of reaction of the epoxy where increasing the heating rate did not allow proper time for the epoxy to react to achieve the optimal properties. Therefore, the curing kinetics of the epoxy does matter and can eliminate the ambiguity of fill and unfilled pores. This influences the final characterization of the coating for supplier qualification and production quality assurance.

6. Future Work

This study shows that the curing kinetics seem to have an impact on the characterization of TBCs. Further experiments at different heating rates below 10 °C/min should be done to find the optimal rate. Vacuum impregnation may be needed for fast heating rates in order to ensure proper impregnation. However, at a slow, controlled heating rate of 2 °C/min, vacuum impregnation may not be necessary. Therefore, with and without vacuum to determine the effects on infiltration of the pores should be studied. On the other hand, in order to increase the accuracy of percent porosity measurements, the grinding and polishing procedures need to be studied in depth as well such as time and pressure.

References

[1] Early Gas Turbine History, *MIT Gas Turbine Laboratory*, [online] 2015, http://web.mit.edu/aeroastro/labs/gtl/early_GT_history.html (Accessed: 15 March 2015).

[2] A. James and S. Rajagopalan, "Gas turbines: operating conditions, components and material requirements," *Elsevier Ltd.*, pp. 3-21, 2014.

[3] J. Dahl, *Wikipedia*, [online] 16 December 2007, http://en.wikipedia.org/wiki/File:Jet_engine.svg (Accessed: 3 February 2015).

[4] J. T. DeMasi-Marcin and D. K. Gupta, "Protective coatings in the gas turbine engine," *Surface and Coatings Technology*, pp. 1-9, 1994.

[5] Journey Through a Jet Engine, *Rolls Royce*, [sound recording], http://html.investis.com/R/Rolls-Royce/corp/interactive-games/journey03/index.html (Accessed: 15 March 2015).

[6] P. Spittle, "Gas turbine technology," *Rolls Royce*, [online] 2003, http://www.iop.org/journals/physed (Accessed: 15 March 2015).

[7] "Tensile Properties," *Vectran Liquid Crystal Polymer Fiber*, [online], http://www.vectranfiber.com/BrochureProductInformation/TensileProperties.aspx (Accessed: 15 March 2015).

[8] "Materials," *MIT*, [online], http://web.mit.edu/course/3/3.082/www/team4_f01/MATERIALS.html (Accessed: 15 March 2015).

[9] "Metal Distributer: Titanium Ti 6Al 4V - AMS 4911," *ASM Space Specification Metals, Inc.*, [online] 2015, http://www.aerospacemetals.com/titanium-ti-6 (Accessed: 15 March 2015).

[10] "Stainless Steel," *Wikipedia*, [online] 2015, http://en.wikipedia.org/wiki/Stainless_steel (Accessed: 11 February 2015).

[11] "Superalloy," *Wikipedia*, [online] 2014, http://en.wikipedia.org/wiki/Superalloy (Accessed: 11 February 2015).

[12] M.Y. He, J.W. Hutchinson, and A.G. Evans, "Simulation of stresses and delamination in a plasma-sprayed thermal barrier system upon thermal cycling," *Materials Science and Engineering A345*, [online] 2003, pp. 172-178, (Accessed: 1 October 2014).

[13] “Thermal spray abradable materials for clearance control coatings,” *Oerlikon*, [online] 2015. http://www.oerlikon.com/metco/en/products-services/coating-materials/thermal-spray/abradables-polymer-fillers/ (Accessed: 15 March 2015).

[14] “What is a thermal barrier coating (TBC)?” *TWI*, [online] 2014. http://www.twi-global.com/technical-knowledge/faqs/material-faqs/faq-what-is-a-thermal-barrier-coating-tbc/ (Accessed: 1 October 2014).

[15] A. Karaoglanli, K. Ogawa, A. Turk, and I. Ozdemir, “Thermal Shock and Cycling Behavior of Thermal Barrier Coatings (TBCs) Used in Gas Turbines.” *InTech*. [online] 2014, Chapter 10, pp 237-260. (Accessed: 1 October 2014).

[16] C. Zhu, A. Javed, P. Li, F. Yang, G.Y. Liang and P. Xiao, “A study of the microstructure and oxidation behavior of alumina/yittria-stablized zirconia (Al_2O_3/YSZ) thermal barrier coatings,” *Surface and Coatings Technology*. [online] 2012. Volume 212, pp 214-222. (Accessed: 1 October 2014).

[17] D.D. Hass, “Thermal barrier coatings via directed vapor deposition,” *Department of Materials Science and Engineering, Vol. PhD. Charlottesville, VA: University of Virginia*, [online] 2001, pp 1-256.(Accessed: 15 March 2015).

[18] Y. Li, C. Li, Q. Zhang, G.J. Yang, and C.X. Li, “Influence of TGO composition on the thermal shock lifetime of thermal barrier coatings with cold-sprayed MCrAlY bond coat,” *ASM International Journal of Thermal Spray Technology*, [online] 2010, Volume 19(1-2), pp 168-177. (Accessed: 1 October 2014).

[19] A. Keyvani, M. Saremi, M. Heydarzadeh, “Oxidation resistance of YSZ-alumina composites compared to normal YSZ TBC coatings at 1100 °C.” *Journal of Alloys and Compounds*. [online] 2011, Volume 509, Issue 33, pp 8370-8377. (Accessed: 1 October 2014).

[20] B. Rashkova, “Microstructural characterization of yttria-stabilized zirconia thermal barrier coatings grown on sapphire substrates,” Ph.D. dissertation, University of Stuttgart, Stuttgart, Germany, 2003.

[21] Z. Lu, S.W. Myoung, Y.G. Jung, G. Balakrishnan, J. Lee, and U. Paik, “Thermal fatigue behavior of air-plasma sprayed thermal barrier coating with bond coat species in cyclic thermal exposure,” Materials, [online] 2013. www.mdpi.com/journal/materials (Accessed: 15 March 2015).

[22] D.R. Clarke, M. Oechsner, and N.P. Padture, “Thermal barrier coatings for more efficient gas turbine engines,” *Materials Research Society Bulletin*, [online] 2012. www.mrs.org/bulletin (Accessed: 15 March 2015).

[23] “Plasma spray process,” *Gordan England*, [online]. http://www.gordonengland.co.uk/ps.htm (Accessed: 15 March 2015).

[24] P.L. Fauchais, "Overview of Thermal Spray," *Thermal Spray Fundamentals From Powder to Part*, Springer US 2013.

[25] "Thermal Spray Coatings," Gordan England, [online]. http://www.gordonengland.co.uk/tsc.htm (Accessed: 15 March 2015).

[26] P. Ctibor, O. Roussel, A. Tricoire, "Unmelted Particles in plasma sprayed coatings ," *Journal of the European Ceramic Society*, [online] 2003. http://www.sciencedirect.com/science/article/pii/S0955221903001043 (Accessed: 15 March 2015).

[27] W.D. Kingry, H.K. Bowen, D.R. Uhlmann, *Introduction to Ceramics*, 2d. ed. New York: Wiley-Interscience, 1976.

[28] M. Hofmann, "Ageing behavior of 3Y-TZP dental ceramics in water, acetic acid and orthophosphoric acid at 80 °C," M.S. thesis, University of Tuebingen, Tubingen, Germany, [online] 2013. http://www.geo.uni-tuebingen.de/studium/studentische-projekte/wissenschaftliches-praesentieren-ss-2013-und-ws-201314/geowissenschaften/martin-hofmann.html (Accessed: 15 March 2015).

[29] "Zirconium Oxide, ZrO_2 Ceramic Properties," *Accuratus*, [online] 2013. http://accuratus.com/zirc.html (Accessed: 15 March 2015).

[30] G. Witz, V. Shklover, and W. Streurer, "Phase evolution in yttria-stabilized zirconia thermal barrier coatings studied by Rietveld refinement of X-Ray powder diffraction patterns," *The American Ceramic Society*, [online] 2007. (Accessed: 15 March 2015).

[31] M. Karger, R. Vaben, and D. Stover, "Atmospheric plasma sprayed thermal barrier coatings with high segmentation crack densities: Spraying process, microstructure and thermal cycling behavior," Surface and Coatings Technology, [online] 2011. http://www.sciencedirect.com/science/article/pii/S0257897211006530 (Accessed: 15 March 2015).

[32] M.F. Smith, D.T. McGuffin, J.A. Henfling, and W.J. Lenling, "A Comparison of Techniques for the Metallographic Preparation of Thermal Sprayed Samples," Journal of Thermal Spray Technology, [online] 1993. http://link.springer.com/article/10.1007%2FBF02650478#page-2 (Accessed: 15 March 2015).

[33] G. Elssner, H. Hoven, G. Kiessler, and P. Wellner, "Ceramics and Ceramic Composites: Materialographic Preparation," *Elesevier*, [online] 1999. https://books.google.com/books?id=U7KIn0tQASAC&pg=PA160&lpg=PA160&dq=metallographic+techniques+for+thermal+barrier+coatings&source=bl&ots=VNaCEXiX8w&sig=GDkyv3Ak0Hy2gqzKllCVsb1DauI&hl=en&sa=X&ei=dFAZVdntNsG6ggSkroPYAw&ved=0CEEQ6AEwBDgK#v=onepage&q=metallographic%20techniques%20for%20thermal%20barrier%20coatings&f=false (Accessed: 15 March 2015).

[34] W.J. Brindley and T.A. Leonhardt, "Metallographic techniques for evaluation of thermal barrier coatings," *Materials Characterization Elsevier*, [online] 1990. http://www.sciencedirect.com/science/article/pii/104458039090029J# (Accessed: 15 March 2015).

[35] M. Kelly, J. Singh, J. Todd, S. Copley, and D.Wolfe, "Metallographic techniques for evaluation of thermal barrier coatings produced by electron beam physical vapor desposition," *Materials Characterization Elsevier*, [online] 2008. http://www.sciencedirect.com.ezproxy.lib.vt.edu/science/article/pii/S1044580307002562 (Accessed: 15 March 2015).

[36] G.V. Voort, "A layman's view of plasma spray coating metallography," Geroge Vander Voort, [online] http://www.georgevandervoort.com/metallography/general/20001238-a-layman-s-view-of-plasma-spray-coating-metallography.html (Accessed: 15 March 2015).

[37] J.J. Friel, "Practical Guide to Image Analysis," ASM International, [online] 2009. http://books.google.com/books?id=8yPBH36M2BQC&pg=PA40&lpg=PA40&dq=what+does+the+epoxy+do+in+metallographic+mounting&source=bl&ots=3dMoWanPdh&sig=IrgFMcgNplDqOMf3ztZ9YnsbXDk&hl=en&sa=X&ei=j3YLVObQGqrbsASd8IKACQ&ved=0CFYQ6AEwBTgU#v=onepage&q=what%20does%20the%20epoxy%20do%20in%20metallographic%20mounting&f=false (Accessed: 15 March 2015).

[38] C. Garschke, P.P Parlevliet, C. Weimer, and B.L. Fox, "Cure kinetics and viscosity modeling of a high-performance epoxy resin film," Polymer Testing Elsevier, [online] 2013. http://www.sciencedirect.com.ezproxy.lib.vt.edu/science/article/pii/S0142941812001900# (Accessed: 15 March 2015).

[39] C. Garschke, C. Weimer, P.P. Parlevliet, and B.L. Fox, "Out-of-autoclave cure cycle study of a resin film infusion process using in situ process monitoring," Composites: Part A Elsevier, [online] 2012. http://www.elsevier.com/locate/compistesa (Accessed: 15 March 2015).

[40] C.L. Lee and K.H. Wei, "Curing kinetics and viscosity change of a two-part epoxy resin during mold filling in resin-transfer molding process," Journal of Applied Polymer Science, [online] 2000. (Accessed: 15 March 2015).

[41] H. Cai, P. Li, G. Sui, Y. Yu, G. Li, X. Y, and S. Ryu, "Curing kinetic study of epoxy resin/flexible amine toughness systems by dynamic and isothermal DSC," Thermochimica Act Elsevier, [online] 2008. http://www.sciencedirect.com/science/article/pii/S0040603108001238 (Accessed: 15 March 2015).

[42] K.S. Jagadeesh, J.G. Rao, K. Shshkikiran, S. Suvarna, S.Y. Amekar, M. Saletore, C. Biswas, A.V. Rajanna, "Cure kinetics of multifunctional epoxies with 2,2' dichloro-4,4'-

diaminodiphenylmethane as hardener," *Journal of Applied Polymer Science*, [online] 2000. http://onlinelibrary.wiley.com/doi/10.1002/1097-4628%2820000906%2977:10%3C2097::AID-APP1%3E3.0.CO;2-4/abstract (Accessed: 15 March 2015).

[43] "Epoxy," Wikipedia, [online] 2015. http://en.wikipedia.org/wiki/Epoxy (Accessed: 15 March 2015).

[44] L. Sun, "Thermal rheological analysis of cure process of epoxy prepeg," Ph.D. dissertation, Louisiana State University and Agricultural and Mechanical College, Louisiana, United Stated, 2002.

[45] "Chemistry of epoxies, epoxy resin, novolacs, and polyurethanes," *Epoxy Products*, [online]. http://www.epoxyproducts.com/chemistry.html (Accessed: 15 March 2015).

[46] "Bisphenol A," *Wikipedia*, [online] 2006. http://commons.wikimedia.org/wiki/File:Bisphenol_A.svg (Accessed: 15 March 2015).

[47] "Bisphenol F," *Wikipedia*, [online] 2006. http://en.wikipedia.org/wiki/Bisphenol#/media/File:Bisphenol_F.svg

[48] J. Abenojar, N. Encinas, J.C. del Real, and M.A. Martinez, "Polymerization kinetics of boron carbide/epoxy composites," *Thermochimica Acta Elsevier*, [online] 2014. http://www.sciencedirect.com.ezproxy.lib.vt.edu/science/article/pii/S004060311300542X (Accessed: 15 March 2015).

[49] "Isophorone diamine," *Chimical Land 21*, [online]. http://www.chemicalland21.com/industrialchem/organic/ISOPHORONE%20DIAMINE.htm (Accessed: 15 March 2015).

[50] "What is the difference between amine, amide, cycloaliphatic, and amine adduct epoxy," *Vanguard Concrete Coating*, [online]. http://www.vanguardconcretecoating.com/types-of-epoxy-resins.htm (Accessed: 15 March 2015).

[52] "Thermogravimetry (TG) or thermogravimetric analysis (TGA) of thermal gravimetric analysis," *Anderson Materials Evaluation, Inc*. [online] 2015. http://www.andersonmaterials.com/tga.html (Accessed: 15 March 2015).

[53] "Thermogravimetric analysis," *Wikipedia*, [online] 2015. http://en.wikipedia.org/wiki/Thermogravimetric_analysis (Accessed: 15 March 2015).

[54] "Q50," *TA Instruments*, [online]. http://www.tainstruments.com/product.aspx?id=21&n=1&siteid=11 (Accessed: 15 March 2015).

[55] “Differential scanning calorimetry,” *Wikipedia*, [online] 2015. http://en.wikipedia.org/wiki/Differential_scanning_calorimetry (Accessed: 15 March 2015).

[56] “Differential scanning calorimetry (DSC) thermal analysis,” *Anderson Materials Evaluation, Inc.*, [online]. http://www.andersonmaterials.com/dsc.html (Accessed: 15 March 2015).

[57] “Differential scanning calorimetry and thermos-gravimetric analysis,” Fleming Polymer Testing and Consulting, [online] 2008. http://www.flemingptc.co.uk/our-services/dsc-tga/ (Accessed: 15 March 2015).

Appendix

Appendix A: Weight Loss and Shrinkage

Initial Weight, g	Cure Temp, °C	Final Weight, g	Weight % Loss
20.90	55	19.83	5.12

Weight loss due to the cross-linking of resin and hardener and release of volatiles

	Diameter, cm	Height, cm	ΔH%	Volume, cm^3	ΔV%
Sample Cup	3.20	3.10	--	24.93	--
Epoxy 55 °C	3.10	2.30	25.81	17.36	30.37
2 °C/min to 55 °C	3.19	2.40	22.58	19.17	23.10

Shrinkage of resin at temperature of 55 °C

Appendix B: Percent Porosity Measurements

Sample	Temp, °C	Avg Porosity Sample 1	Avg Porosity Sample 2	Avg Porosity Sample 3
2 °C/min	55	29.33	33.08	27.55
5 °C/min	55	39.30	--	37.80
10 °C/min	55	27.06	25.83	--
No Rate	55	17.30	26.18	33.61
2 °C/min	70	25.60	--	26.09
5 °C/min	70	31.68	20.14	--
10 °C/min	70	--	--	--
No Rate	70	--	--	29.09

Porosity measurements for samples without prior heating of epoxy

Sample	Temp, C	Avg Porosity Sample 1	Avg Porosity Sample 2	Avg Porosity Sample 3
2 °C/min	55 H	--	25.44	--
5 °C/min	55 H	35.42	--	--
10 °C/min	55 H	34.09	41.85	30.66
No Rate	55 H	32.61	27.73	31.93
2 °C/min	70 H	17.42	--	15.89
5 °C/min	70 H	--	--	--
10 °C/min	70 H	17.82	19.55	15.36
No Rate	70 H	25.98	28.27	27.52

Porosity measurements for samples with prior heating of epoxy